RESEARCH OUTPUTS / RÉSULTATS DE RECHERCHE

Plasma membrane nanodeformations promote actin polymerization through CIP4/CDC42 recruitment and regulate type II IFN signaling

Ledoux, Benjamin; Zanin, Natacha; Yang, Jinsung; Mercier, Vincent; Coster, Charlotte; Dupont-Gillain, Christine; Alsteens, David; Morsomme, Pierre; Renard, Henri François

[Link to publication](#)

CELL BIOLOGY

Plasma membrane nanodeformations promote actin polymerization through CIP4/CDC42 recruitment and regulate type II IFN signaling

Benjamin Ledoux[1,2,3], Natacha Zanin[4], Jinsung Yang[5], Vincent Mercier[6], Charlotte Coster[1], Christine Dupont-Gillain[7], David Alsteens[2], Pierre Morsomme[1]*, Henri-François Renard[3,4]*

In their environment, cells must cope with mechanical stresses constantly. Among these, nanoscale deformations of plasma membrane induced by substrate nanotopography are now largely accepted as a biophysical stimulus influencing cell behavior and function. However, the mechanotransduction cascades involved and their precise molecular effects on cellular physiology are still poorly understood. Here, using homemade fluorescent nanostructured cell culture surfaces, we explored the role of Bin/Amphiphysin/Rvs (BAR) domain proteins as mechanosensors of plasma membrane geometry. Our data reveal that distinct subsets of BAR proteins bind to plasma membrane deformations in a membrane curvature radius–dependent manner. Furthermore, we show that membrane curvature promotes the formation of dynamic actin structures mediated by the Rho GTPase CDC42, the F-BAR protein CIP4, and the presence of PI(4,5)P$_2$. In addition, these actin-enriched nanodomains can serve as platforms to regulate receptor signaling as they appear to contain interferon-γ receptor (IFNγ-R) and to lead to the partial inhibition of IFNγ-induced JAK/STAT signaling.

INTRODUCTION

In their environment, cells constantly encounter diverse external mechanical stimuli and stresses that cause membrane curvature and cell deformation, requiring appropriate responses. Of these, cell deformation caused by nanoscale topographical features of the culture substrate has been shown to alter key cellular functions such as adhesion (*1*, *2*), differentiation (*3*–*5*), proliferation (*6*, *7*), and migration (*8*). In parallel, plasma membrane curvature has been shown to influence several molecular processes, including focal adhesion formation (*1*, *8*, *9*), clathrin-mediated endocytosis (*10*, *11*), and actin polymerization (*12*, *13*). However, numerous gaps remain in the understanding of these molecular mechanisms and their connection with changes in cellular behavior. In particular, it is still not known how cells are able to sense and discriminate various types of deformations in terms of size, geometry, and dynamics, leading them to finely tailor their responses.

Because of their properties, it is not surprising to find Bin/Amphiphysin/Rvs (BAR) domain proteins as main players of these dynamic molecular machineries. Multiple recent studies have shown that BAR domain proteins play pivotal roles in membrane geometry recognition and processing (*10*, *12*, *14*–*17*). BAR domain proteins form crescent-shaped dimers with a unique intrinsic curvature radius, allowing them to induce and/or bind membrane deformations of different geometries. They are classified into several subfamilies mainly on the basis of their structures and associated domains. Generally, N-BARs (containing an N-terminal amphipathic helix) exhibit a pronouncedly curved structure, whereas Fes/CIP4 homology BARs (F-BAR) display a comparatively shallower curvature (*18*–*20*). Then, after binding membranes through their BAR domain, they can promote local molecular responses due to the presence of additional functional domains such as Src homology 3 (SH3) or Rho guanosine triphosphatase (GTPase)–activating protein (GAP) domains. In particular, F-BAR domain proteins from the transducer of CDC42-dependent actin assembly (TOCA) subfamily (CIP4, FBP17, and FNBP1L) have been linked to the remodeling of the actin cytoskeleton through activation of N-WASP and Arp2/3 in response to topography-induced membrane curvature (*12*). However, the regulation and the purpose of this actin reorganization are still largely unknown. CIP4 and FBP17, together with the Rho GTPase CDC42, have also been involved in the priming step of fast endophilin-mediated endocytosis (FEME) carriers, another membrane curvature–driven process that does not rely on clathrin (*21*).

In this study, we developed an efficient colloidal lithography technique to synthesize fluorescent nanostructured substrates that were used to induce spherical and isotropic nanoscale plasma membrane deformations ranging from 100 to 500 nm in living cells. Using this tool in combination with high-resolution confocal microscopy, we showed that a distinct subset of BAR domain proteins was recruited to each plasma membrane deformation size. The affinity of BAR proteins for a particular curvature radius does not correlate with their usual subfamily classification. Our data further demonstrate that membrane curvature promotes the formation of dynamic actin structures mediated by the Rho GTPase CDC42 (and not Rac1), the F-BAR protein CIP4, and the presence of

phosphatidylinositol 4,5-bisphosphate [PI(4,5)P_2]. Furthermore, using correlative fluidic force microscopy (FluidFM)/fast-scanning confocal microscopy, we demonstrated that these actin structures can form at both basal and apical plasma membranes in a very dynamic manner. In addition, the membrane nanodomains induced by the largest nanostructures (500 nm) are independent of clathrin and resemble early-stage FEME-like endocytic pits. This opens up the exciting possibility of the existence of frustrated clathrin-independent endocytosis, reminiscent of the previously described frustrated clathrin-mediated endocytosis (22–24). Moreover, these actin-enriched nanodomains harbor interferon-γ receptors (IFNγ-Rs) with impaired signaling. Together, our data demonstrate that plasma membrane deformation induces the formation of CDC42/CIP4/PI(4,5)P_2-dependent actin structures and that large actin rings induced by substrate nanotopography can modulate receptor signaling.

RESULTS

Nanostructured cell culture substrates synthesized by colloidal lithography can generate nanoscale deformations of plasma membrane

Multiple nanofabrication techniques exist to create a variety of nanopatterns used for the study of cellular responses to membrane deformations. While some are limited by their complexity and/or low throughput [e.g., electron beam lithography and focused ion beam (FIB)], others are relatively simple to work with. Here, we took advantage of both the rapidity and simplicity of colloidal lithography to produce substrates featuring fluorescent spherical nanostructures (25). Briefly, negatively charged spherical silica colloids were coated with a positively charged polymer, polyallylamine (PAH) (Fig. 1A). The added amine groups were then functionalized using succinimidyl ester–conjugated fluorescent dyes (ATTO 390, Alexa Fluor 488, Alexa Fluor 555, or ATTO 647N), leading to the generation of fluorescent colloids. Next, these colloids were adsorbed onto a glass coverslip to create the nanostructures (Fig. 1A). Last, the substrate was coated with collagen to make the surface chemistry uniform with stable nanostructures and appropriate cell adhesion properties (Fig. 1A). This approach allowed the quick and cost-effective patterning of relatively large surfaces for cell culture (12- and 30-mm round coverslips) with fluorescent nanostructures of 500, 300, and 100 nm in nominal diameter at various densities (Fig. 1, B and C). Despite their small size and random distribution, the nanostructures are easily distinguished on the substrate because of their fluorescence. In addition, unlike commercial fluorescent polystyrene beads, our nanostructures offer the advantage of matching the surface chemistry and stiffness of the underlying glass substrate, eliminating potential effects caused by substrate heterogeneity.

When cells were seeded on nanostructured substrates, the plasma membrane underwent deformation and wrapped around the nanostructures, as visualized by FIB–scanning electron microscopy (SEM) (Fig. 1, D to I, and fig. S1A). As expected, plasma membrane closely followed the spherical shape of individual nanostructures (Fig. 1, D to I). For 500-nm nanostructures, plasma membrane matched tightly their shape most of the time, giving rise to an omega-shaped membrane curvature (Fig. 1, D and E). Regarding 300- and 100-nm nanostructures, plasma membrane was deformed isotropically on the top and sides of the

particles, but these geometries were less prone to induce omega-shaped membrane curvature (Fig. 1, F to I). Overall, plasma membrane deformations seemed to match well the shape of the nanostructures used, whatever their size. Furthermore, across all nanostructure sizes, we observed a negative curvature of the plasma membrane at the interface between the particles and the underlying flat coverslip (Fig. 1, D to I). We then further confirmed the wrapping of plasma membrane using high-resolution Airyscan confocal microscopy by expressing a palmitoylated and myristoylated (PalMyr)–green fluorescent protein (GFP) as a plasma membrane marker (Fig. 1J, green channel). In addition, the actin cytoskeleton reacted to this curvature and underwent reorganization, forming actin rings (Fig. 1J, red channel). Both membrane wrapping and actin ring structures were observable on nanostructures of 500 and 300 nm (Fig. 1J and fig. S1, B and C). On 100-nm nanostructures, because of the resolution limit of Airyscan microscopy, local actin polymerization appeared as dots rather than rings (fig. S1C). However, using super-resolution stimulated-emission-depletion (STED) nanoscopy, we confirmed that those dots observed in Airyscan were indeed unresolved actin rings (fig. S1D). Although the nanostructures are not covalently bound to the surface, they were mostly stable and neither displaced nor internalized by cells for a minimum of 2 hours after cell seeding (movie S1). Together, these data underline the relevance of our nanostructured substrate to study biomolecular mechanisms triggered by plasma membrane bending.

BAR domain proteins bind to plasma membrane deformations in a membrane curvature radius–dependent manner

To investigate how cells can detect and respond to nanoscale curvature of their plasma membrane, we conducted a quantitative screening, focusing on BAR domain protein affinity for membrane deformations of 500, 300, and 100 nm (Fig. 2, A to E). Because of their curved shape and their ability to sense membrane curvature, BAR domain proteins are ideal candidates to connect plasma membrane geometry to downstream cellular responses. Of note, some BAR domain proteins have already been involved in such mechanisms (14, 10, 12, 26). To identify which BAR domain proteins could be potential candidates in mechano-transduction responses, HeLa cells transiently expressing fluorescently tagged BAR domain proteins (69 constructs screened) were seeded on nanostructured substrates for 1 hour and fixed. Cells were then imaged using high-resolution Airyscan confocal microscopy (fig. S2), and the fluorescence around each individual nanostructure was quantified using a homemade (semi-)automated method (Fig. 2, A to D, and fig. S3). Juxtaposed or aggregated nanostructures were automatically discarded from the quantification. In brief, the level of fluorescence around membrane deformations was expressed as an enrichment ratio (see fig. S3 and Materials and Methods for details about the quantification procedure). This ratio represents the increase in fluorescence intensity around nanostructures as compared to the distant undeformed/flat membrane. A log_{10} transformation was subsequently applied to normalize the data, aiming to achieve Gaussian distributions and enhance the robustness of statistical analyses. A positive value indicates that, on average, there is an increase in fluorescence around membrane deformations. As a negative control, we used PalMyr-GFP to take into account the nonspecific gain in fluorescence due to the bending
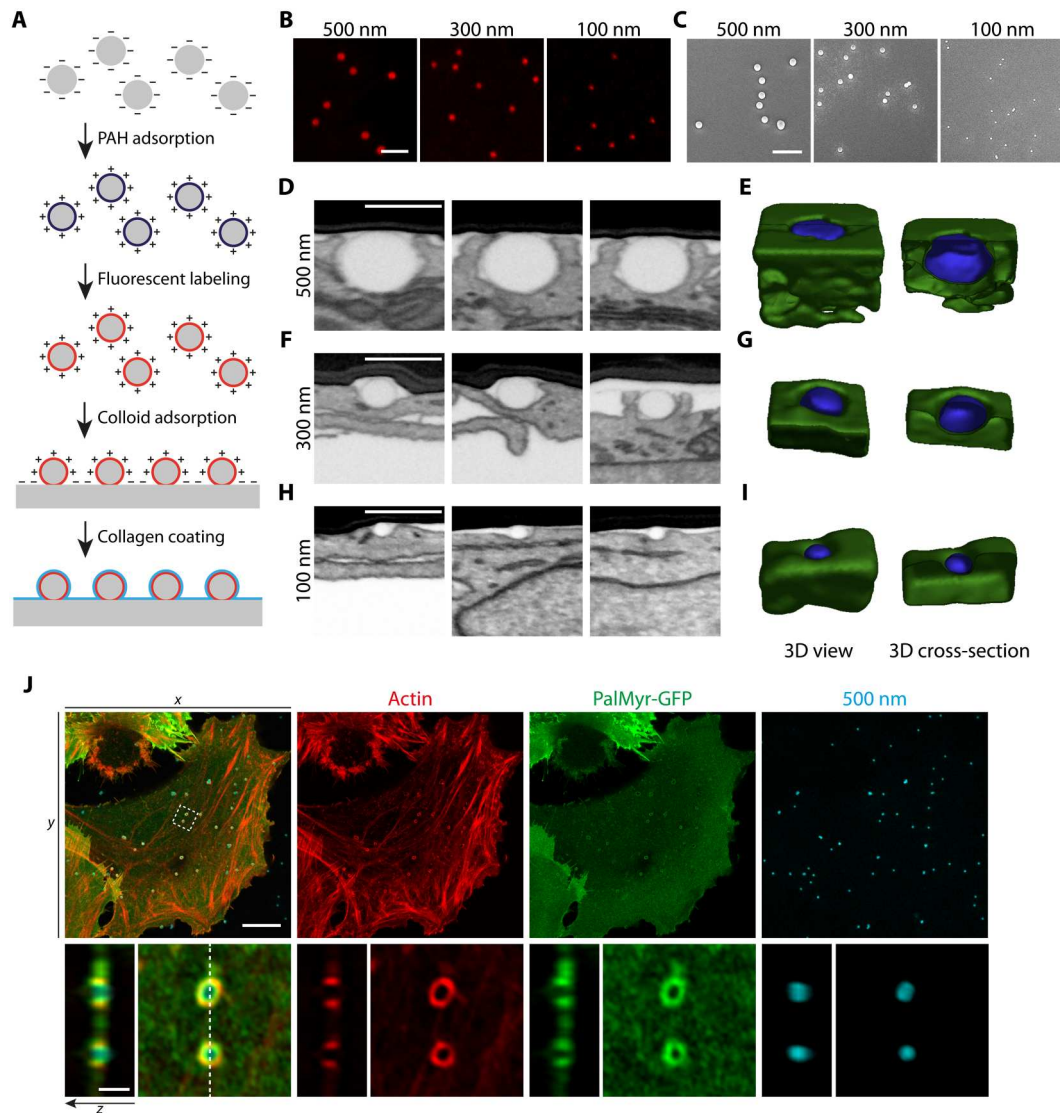
Fig. 1. Nanostructures deform cell plasma membrane and induce local actin polymerization. (**A**) Synthesis of nanostructured substrates. Silica colloids were coated with PAH, labeled with fluorescent dyes, and adsorbed onto coverslips. Coverslips were then coated with collagen before seeding cells. (**B** and **C**) ATTO 390–labeled nanostructures of 500, 300, and 100 nm visualized by Airyscan confocal microscopy (B) or SEM (C). (**D** to **I**) FIB-SEM images [(D), (F), and (H)] and 3D reconstructions [(E), (G), and (I)] of plasma membrane deformed by individual nanostructures. Plasma membrane, green; nanostructure, blue. Uncropped FIB-SEM images in fig. S1A. (**J**) HeLa cells expressing PalMyr-GFP (green) seeded on 500-nm nanostructures (cyan) and stained for actin (phalloidin, red). Region marked by a dashed square, expanded below [(J), bottom], and also displayed as a transversal view along the Z axis. Representative images from >3 independent experiments [(B) and (J)] or a single experiment [(C) to (I)]. Scale bars, 10 μm [(J), top], 2 μm [(B) and (C)], 1 μm [(J), bottom], and 500 nm [(D), (F), and (H)].

of the membrane perpendicularly to the focal plane. BAR proteins with an enrichment ratio significantly higher than PalMyr-GFP were considered as specifically enriched, thus having a higher affinity for the corresponding deformation (Fig. 2, A to D).

We observed that different subsets of BAR proteins were recruited according to the size of the deformations (Fig. 2D). Although some were recruited independently of the size of the deformation (e.g., PSTPIP1 and PACSIN3), others displayed more specificity toward smaller/larger sizes (e.g., CIP4 toward 100 nm). However, some discrepancies in the local accumulation at the plasma membrane were observed between the fusion proteins expressing the full BAR protein sequence versus the BAR domain alone. For instance,

we observed that srGAP1-3 BAR domains alone were highly recruited to deformations, while recruitment was barely observable for the full-length proteins. This might be due to autoinhibition of the BAR domain by the SH3 domain, as it was previously shown in the case of srGAP2 (*27*). In addition, according to our assumptions, we detected a local accumulation of most BAR proteins that were previously studied for their curvature sensing ability such as Nadrin2, FCHo1, CIP4, FNBP1L, and FBP17 (*10, 12, 14*).

Unexpectedly, the affinity of BAR domain proteins for a specific membrane curvature radius was not found to correlate with their intrinsic protein curvature radius, typically represented by their subfamily classification. Some members of both F-BAR and N-
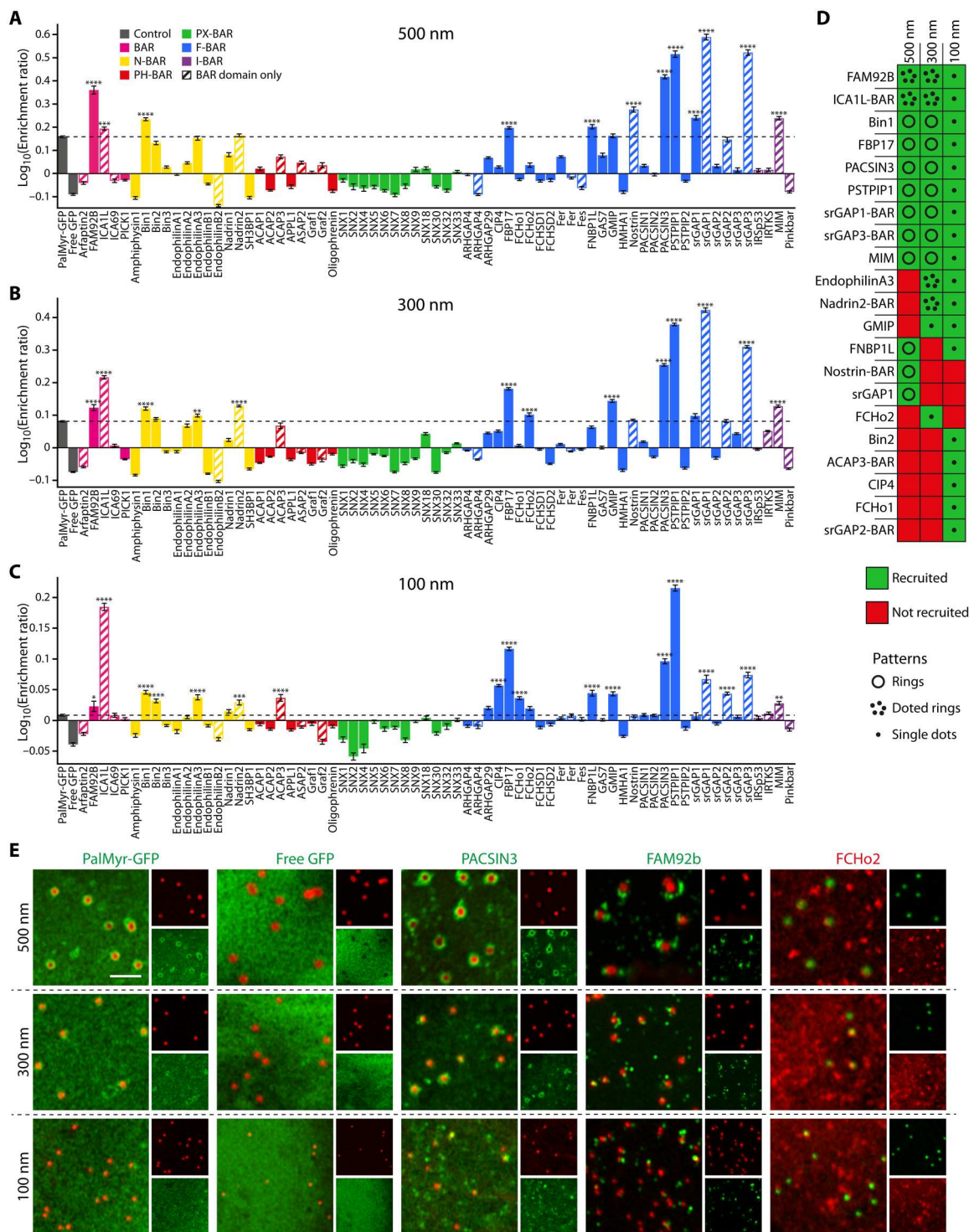
Fig. 2. BAR domain proteins bind to plasma membrane deformations in a membrane curvature radius–dependent manner. (**A** to **C**) Quantification of Airyscan images showing the recruitment of fluorescently tagged BAR domain proteins to 500 nm (A), 300 nm (B), and 100 nm (C) plasma membrane deformations in HeLa cells (more details on the quantification procedure in fig. S3). Data are means ± SEM from two independent experiments with a minimum of 158 deformations per construct (see table S1 for exact *n* for each condition). Each protein was compared to the recruitment of PalMyr-GFP used as a control (dashed lines). ****$P < 0.0001$; ***$P < 0.001$; **$P < 0.01$; *$P < 0.05$ [one-way analysis of variance (ANOVA) with Dunnett's multiple comparison test]. (**D**) Summary table of recruited BAR domain proteins and their patterns. (**E**) Representative images of controls (PalMyr-GFP and GFP) and selected BAR domain proteins depicting different patterns observed around membrane deformations. Representative images for each condition in fig. S2. Scale bar, 2 μm (E).

BAR subfamilies were observed to be recruited to nanodeformations of all tested curvature sizes. This observation may appear rather counterintuitive, as N-BAR domains are usually considered to favor much higher membrane curvature than F-BAR domains (*18*, *19*). Furthermore, we also observed the recruitment of the BAR domain of an inverse BAR (I-BAR) protein, MIM (Fig. 2, A to C). To determine the location of BAR proteins more accurately along the Z axis of the nanodeformations, we acquired Z-stacks of cells seeded on 500-nm nanostructures and transiently expressing some representative members of different BAR subfamilies: PACSIN3 for F-BAR, Bin1 for N-BAR, and the BAR domain of MIM for I-BAR (fig. S4, A and B). For each protein, several images of deformations were averaged to create heatmaps of protein enrichment at various Z positions (fig. S4B). These enrichment ratios were further normalized to determine the relative enrichment at each Z position (fig. S4A). At the resolution of Airyscan (axial resolution of 350 nm), MIM appeared more favorably recruited closer to the bottom of nanostructures, where they contact the coverslip (fig. S4, A and B). This is likely where the membrane forms a saddle point and negative curvature can be

observed (see Fig. 1, D and E). On the other hand, Bin1 rather preferred the top part of nanostructures, while PACSIN3 appeared more evenly distributed, like PalMyr-GFP (fig. S4, A and B). These results suggest that BAR domain proteins from different subfamilies are recruited to different Z positions, according to the various membrane curvatures existing along the Z axis. Of note, these observations may partly explain why we observed no apparent correlation between the radius of nanostructures and the intrinsic curvature radius of BAR domains.

At the resolution of Airyscan, we were able to visually distinguish three clear patterns around deformations among the 21 hits: uniform rings, single dots, or clusters of dots surrounding individual deformations (Fig. 2, D and E). These patterns seem to be protein specific as proteins forming rings (e.g., PACSIN3 and PSTPIP1) or clusters of dots (e.g., FAM92B and EndophilinA3) did so on both 500 and 300 nm. Of note, single dots were probably unresolved rings or clusters of dots as they appeared mostly around 100-nm deformations. To obtain a more precise view of the dynamics standing behind clusters of dots, we performed live imaging on 500-nm nanostructures with cells expressing GFP-tagged

Downloaded from https://www.science.org on February 05, 2024
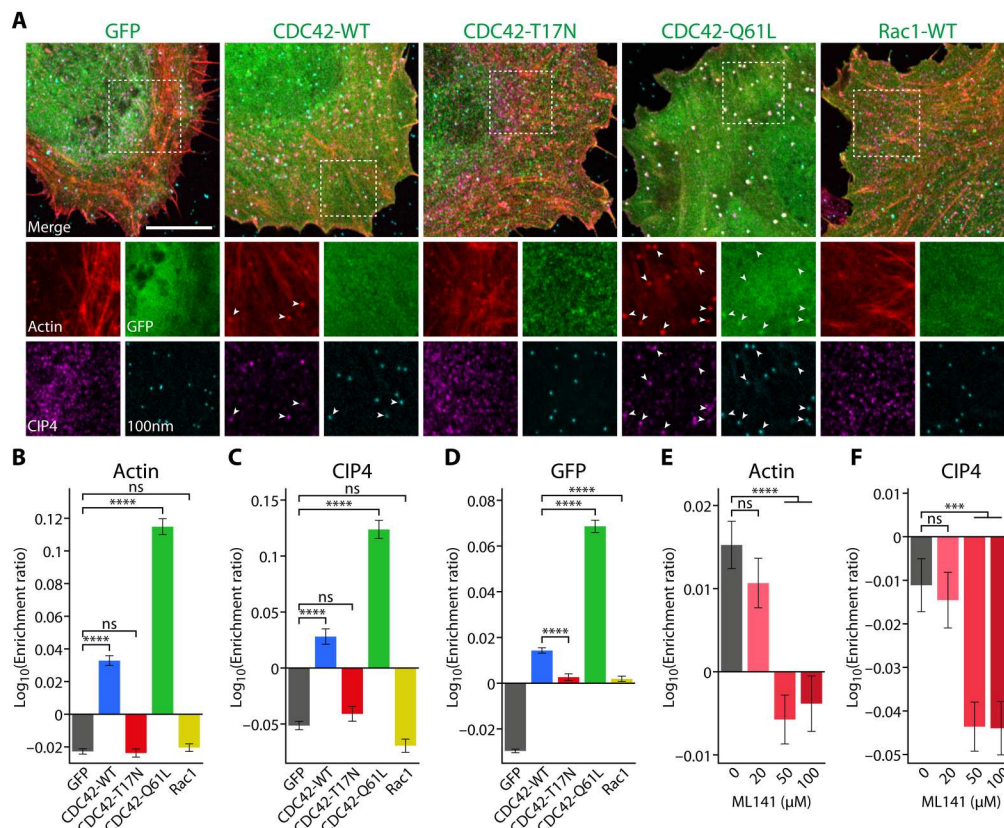
Fig. 3. CDC42 controls actin polymerization and CIP4 recruitment around 100-nm plasma membrane deformations. HeLa cells grown on 100-nm nanostructures and transfected with fluorescent constructs [(A) to (F)] or treated with a specific CDC42 inhibitor (ML141) [(E) and (F)], as indicated. Data shown are quantifications of actin [(B) and (E)], endogenous CIP4 [(C) and (F)], or GFP (F) fluorescence around 100-nm deformations and the corresponding representative Airyscan images (A). (**A** to **D**) Effect of transient expression of GFP, GFP-CDC42-WT, GFP-CDC42-T17N, GFP-CDC42-Q61L, or GFP-Rac1-WT on the enrichment of actin, CIP4, and GFP around deformations. Number of deformations: GFP, $n = 8146$; CDC42-WT, $n = 3829$; CDC42-T17N, $n = 2993$; CDC42-Q61L, $n = 3058$; Rac1-WT, $n = 3942$. Three independent experiments. (**E** and **F**) Effect of dose-dependent inhibition of CDC42 by ML141 (0, 20, 50, or 100 μM) on the enrichment of actin and CIP4 around deformations. Number of deformations: 0 μM, $n = 3007$; 20 μM, $n = 2541$; 50 μM, $n = 2788$; 100 μM, $n = 2252$. Three independent experiments. Data are means ± SEM; ns, not significant; ****$P < 0.0001$; ***$P < 0.001$ (one-way ANOVA with Dunnett's multiple comparison test). Regions marked by dashed squares, expanded below with individual channels displayed (A, bottom). White arrowheads, colocalization (A). Scale bars, 10 μm (A).

EndophilinA3, a BAR protein previously involved in clathrin-independent endocytosis (28). In agreement with previous reports (28, 29), we observed that EndophilinA3 was transiently recruited to plasma membrane and displayed a dynamic punctate pattern (fig. S5, A and B). As in the screening (fig. S2), we observed the typical dotted pattern at the periphery of nanostructures when looking at single frames (fig. S5A). However, unexpectedly, EndophilinA3 seemed more frequently recruited to 500-nm deformations than to the distant flat membrane, as observed on the time projection image showing where EndophilinA3 spots appeared preferentially at the cell surface (fig. S5B). Therefore, the dotted pattern that we observed for some hits in our screening may result from a short protein lifetime around membrane deformations. Together, these results indicate that cells are able to use distinct arsenals of BAR domain proteins to discriminate different plasma membrane deformation geometries.

CDC42 drives the recruitment of CIP4 and polymerization of the actin cytoskeleton around plasma membrane deformations

A closer look at the screening results (Fig. 2, A to D) revealed several hits that are already known to play a role in cytoskeleton reorganization and Rho GTPase signaling (srGAPs, TOCAs, Nadrins, and GMIP) (30). In particular, TOCA proteins (CIP4, FBP17, and FNBP1L) are well-known effectors of CDC42 and seem to be involved in curvature-mediated actin polymerization (12). However, it remains unknown whether CDC42 plays any role in this curvature-mediated remodeling of the actin cytoskeleton.

To answer this question, we first explored the effect of transient expression of wild-type CDC42 (CDC42-WT) as well as its constitutively active (CDC42-Q61L) or dominant-negative (CDC42-T17N) mutants (Fig. 3, A to D). When wild-type CDC42 was overexpressed, we observed an increase in both actin polymerization and CIP4 recruitment to 100-nm deformations (Fig. 3, A to D). Furthermore, upon expression of the active CDC42-Q61L mutant, the recruitment of actin and CIP4 was even more pronounced, with the appearance of actin structures around most deformations (Fig. 3, A to C). In addition, we observed that CDC42-WT and its active mutant are both recruited to the deformations (Fig. 3, A and D). In contrast, neither CDC42-T17N mutant nor Rac1 affected CIP4 and actin recruitment (Fig. 3, A to C). As expected, CDC42, CIP4, and actin were almost systematically found colocalizing around the deformations (Fig. 3, A to D, white arrowheads). Similar results were observed with 300- and 500-nm deformations (figs. S6, A to D, and S7, A to D): The expression of CDC42-Q61L increased local actin polymerization and CIP4 recruitment, while CDC42-T17N had the opposite effect. Nevertheless, the effect was more pronounced for 100-nm deformations, with the formation of big patches of CIP4 and actin near individual deformations. Using STED nanoscopy to circumvent the resolution limit of Airyscan, we confirmed that CIP4 and actin were indeed recruited nonrandomly to 100-nm deformations in control cells (fig. S8). Next, the results obtained with CDC42 dominant-negative mutant were confirmed using the drug ML141, a specific inhibitor of CDC42 Rho GTPase activity. Cells treated with this compound showed a reduced CIP4 recruitment and actin polymerization around all deformation sizes in a dose-dependent manner (Fig. 3, E and F, and figs. S6, E and F, and S7, E and F). These observations suggest that

CDC42 controls both local actin polymerization and CIP4 recruitment.

In agreement with the previous data using CDC42 mutants and pharmacological inhibitor ML141, the knockdown of CDC42 completely abolished the local actin polymerization on all deformation sizes (Fig. 4, A and B, and figs. S6, G and H, and S7, G and H). In addition, the depletion of CIP4 only slightly reduced actin polymerization on 100-nm deformations (Fig. 4, A and B). This effect was strongly enhanced by the concomitant depletion of all three TOCA family members, indicating that functional redundancy might exist between the three proteins (Fig. 4, A and B). No significant effect or only a slight reduction of actin polymerization was observed upon CIP4 and all TOCA protein depletion around 300- and 500-nm deformations, respectively (figs. S6, G and H, and S7, G and H). Rac1, clathrin, or μ2-adaptin (encoded by *AP2M1* gene) depletions did not significantly decrease actin polymerization on 300- and 500-nm deformations (figs. S6H and S7H). However, while Rac1 and clathrin knockdown led only to a partial inhibition of actin polymerization on 100-nm deformations, μ2-adaptin depletion led to an inhibition level similar to CDC42 depletion (Fig. 4B). Besides, immunofluorescence experiments showed no significant accumulation of clathrin around membrane deformations, and clathrin signal did not correlate with actin enrichment (fig. S9, A to F). Of note, depletion was validated by Western blot experiments (Fig. 4C). Together, these data indicate that, while clathrin machinery is not involved in actin polymerization on bigger deformation sizes (300 and 500 nm), we cannot exclude an indirect involvement on smaller sizes (100 nm).

To further confirm the involvement of TOCA proteins in the described mechanism, we transiently expressed each member of the family and measured actin polymerization around deformations. All constructs increased actin polymerization around 100-nm deformations (Fig. 4, D and E), while no effect was observed around 300- or 500-nm deformations (figs. S6, I and J, and S7, I and J). Afterward, to get more insights into the molecular functions of CIP4, we performed rescue experiments by expressing fluorescently tagged truncation mutants of the protein in cells previously depleted of all endogenous TOCAs before seeding them on 100-nm nanostructured substrates (Fig. 4, F to I). Only full-length CIP4 was able to rescue actin polymerization on 100-nm deformations (Fig. 4G). The removal of any part of the protein resulted in the loss of its ability to promote curvature-induced actin polymerization. The various truncated versions were differently recruited to the nanodeformations (Fig. 4H). While truncation of the SH3 domain (ΔSH3) barely affected the recruitment of the protein, removing the REM1 domain (ΔREM1) and/or the basic region (ΔBasic) had a strong effect (Fig. 4H). Of note, the F-BAR domain alone (F-BAR) was not recruited at all to the deformations, and addition of the small basic region to it (F-BAR⁺) was sufficient to increase its recruitment level (Fig. 4H), although still far from the full-length protein or the ΔSH3 mutant. However, to reach a recruitment level to the nanodeformations closer to the wild-type CIP4, it appears that the REM1 domain is essential (comparing the F-BAR⁺ and ΔSH3 conditions; Fig. 4H). Together, these results suggest that the basic region of CIP4 is important for its binding to the plasma membrane and that the REM1 domain plays a crucial role in the specific recruitment of CIP4 to the nanodeformations. As the REM1 domain is described to mediate CIP4 interaction with CDC42-GTP (guanosine triphosphate) (31), our findings thus strongly suggest that this
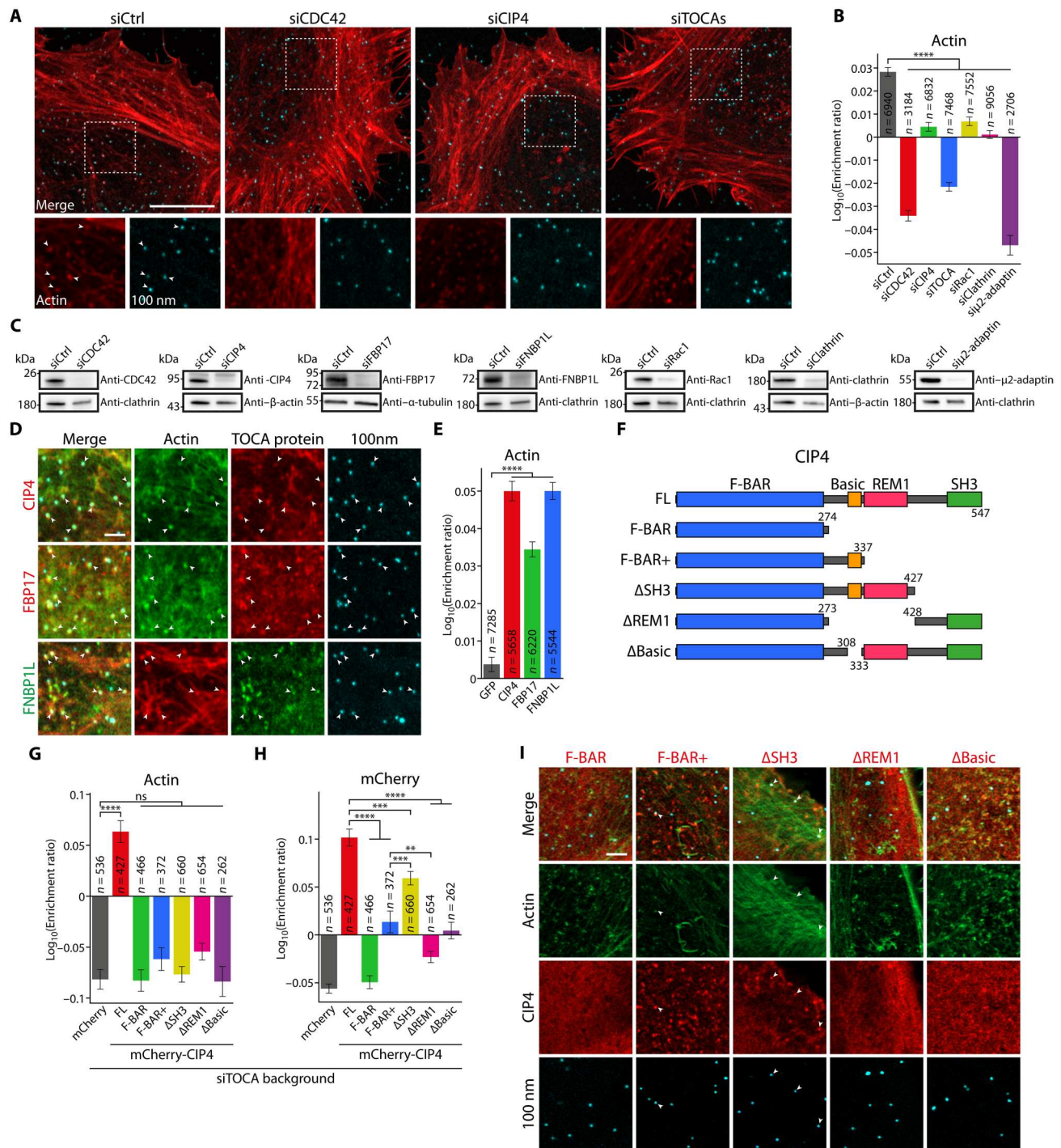
Fig. 4. CIP4 controls actin polymerization around 100-nm plasma membrane deformations. HeLa cells grown on 100-nm nanostructures and treated with siRNAs [(A) to (C) and (G) to (I)] and/or transfected with constructs [(D), (E), and (G) to (I)]. Quantifications of actin [(B), (E), and (G)] or mCherry (H) fluorescence around 100-nm deformations and corresponding representative Airyscan images [(A), (D), and (I)]. (**A** and **B**) Effect of CDC42, CIP4, TOCAs (CIP4, FBP17, and FNBP1L), Rac1, clathrin heavy chain, or μ2-adaptin depletion with siRNAs on actin enrichment around deformations. Regions marked by dashed squares, expanded below with individual channels displayed (A, bottom). (**C**) Immunoblots of CDC42, CIP4, FBP17, FNBP1L, Rac1, clathrin heavy chain, and μ2-adaptin document siRNA knockdown efficiency (uncropped blots, see fig. S13). (**D** and **E**) Effect of transient expression of GFP or individual TOCA proteins (mCherry-CIP4, mCherry-FBP17, or GFP-FNBP1L) on actin enrichment around deformations. (**F**) CIP4 truncation mutants (mCherry-tagged). FL, full-length protein; F-BAR, BAR domain only; F-BAR+, BAR domain with basic region; ΔSH3, lacking SH3 domain; ΔREM1, lacking basic region and REM1 domain; ΔBasic, lacking basic region. (**G** to **I**) Rescue experiment. Transient expression of free mCherry, mCherry-tagged full-length CIP4, or truncation mutants in cells where endogenous TOCA proteins are depleted. Number of independent experiments, three [(A), (B), and (G) to (I)] or four [(D) and (E)]. Number of deformations (n) depicted on each graph. Data are means ± SEM; ****$P < 0.0001$; ***$P < 0.001$; **$P < 0.01$ [one-way ANOVA with Dunnett's [(B), (E), and (G)] or Tukey's (H) multiple comparison test]. White arrowheads, colocalization [(A), (D), and (I)]. Scale bars, 10 μm (A) and 2 μm [(D) and (I)].

interaction is necessary for the specific recruitment of CIP4 to the plasma membrane nanodeformations. In addition, although ΔSH3 CIP4 was recruited to the nanodeformations, it was unable to restore local actin polymerization. Therefore, our results further indicate that the SH3 domain of CIP4 is crucial for the activity of the protein in the regulation of actin polymerization rather than for the recruitment of CIP4 to the nanodeformations. This also demonstrates that CIP4 recruitment occurs upstream of actin polymerization.

Together, these observations suggest that activated CDC42 recruits CIP4 (or other TOCA proteins) locally to plasma membrane nanodeformations, where both proteins cooperate to induce subsequent local actin polymerization. This CDC42-TOCA protein system seems to be highly curvature sensitive, as it appears strictly required for local actin polymerization on the smaller size deformations (100 nm), while not on larger sizes (300 and 500 nm). More precisely, although CDC42 seems to be important for actin ring

formation around all deformation sizes, TOCAs are strictly required only on 100-nm deformations. This indicates that other partners may participate in controlling actin polymerization around larger membrane deformations. Moreover, the formation of actin rings induced by larger nanostructures (300 and 500 nm) appears to be independent of clathrin machinery.

To identify the players involved in actin ring formation, we further investigated the regulation of CDC42, focusing on Rho GAP domain–containing proteins, since some of them are also known to be part of the BAR domain protein superfamily. Briefly, we individually depleted Nadrin1/2, Oligophrenin, and srGAP1/2/3 and monitored actin polymerization around 500-nm plasma membrane nanodeformations (fig. S10, A and B). Although some of these proteins did not show any obvious enrichment around the deformations in the previous screening (see Fig. 2A), the depletion of Nadrin2, Oligophrenin, and srGAP3 significantly increased actin polymerization (fig. S10, A and B). These observations suggest
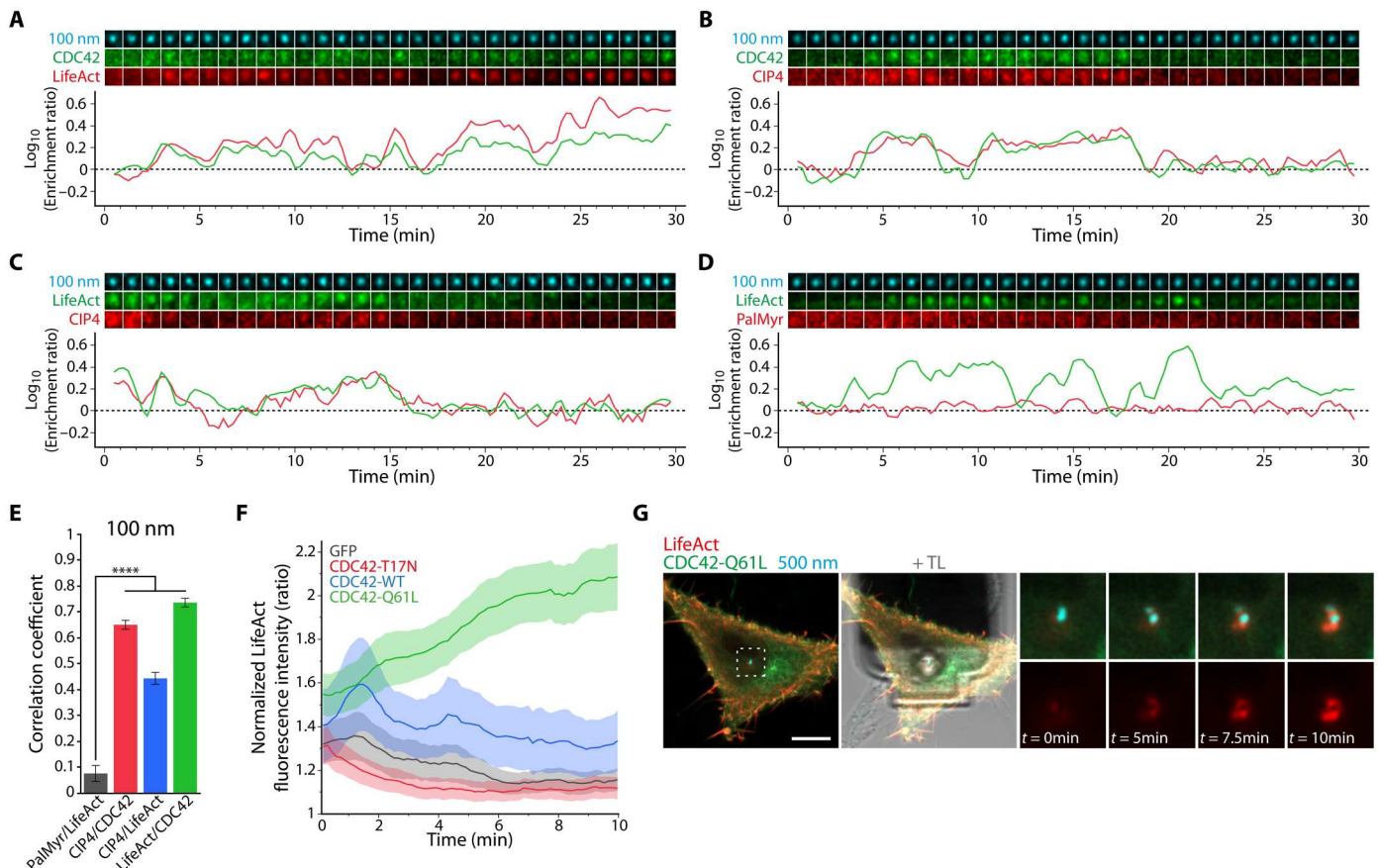
Fig. 5. Local CIP4- and CDC42-dependent actin polymerization is dynamic and promoted by plasma membrane curvature. (**A** to **D**) Representative Airyscan time lapses and corresponding quantifications of enrichment ratios of the following pairs around 100-nm deformations over time: (A) GFP-CDC42 and LifeAct-mCherry, (B) GFP-CDC42 and mCherry-CIP4, (C) LifeAct-GFP and mCherry-CIP4, and (D) LifeAct-GFP and PalMyr-mCherry (PalMyr). Thirty-minute time-lapses with 15-s intervals between frames. Region size, 0.85 μm. (**E**) Correlation coefficients between the pairs of proteins shown in (A) to (D). Number of deformations: PalMyr/LifeAct, $n = 65$; CIP4/CDC42, $n = 118$; CIP4/LifeAct, $n = 83$; LifeAct/CDC42, $n = 145$. Three independent experiments. (**F** and **G**) Monitoring of CDC42-dependent actin polymerization upon deformation of the plasma membrane by FluidFM. (F) Quantification of normalized LifeAct-mCherry fluorescence intensity around FluidFM tip over time upon coexpression of GFP (control, black), GFP-CDC42-T17N (red), GFP-CDC42-WT (blue), or GFP-CDC42-Q61L (green). Ten-minute time-lapses with 9-s intervals between frames. Number of cells: GFP, $n = 20$; GFP-CDC42-T17N, $n = 18$; GFP-CDC42-WT, $n = 15$; GFP-CDC42-Q61L, $n = 17$. Two independent experiments. (G) Representative image of FluidFM/confocal experiments upon coexpression of GFP-CDC42-Q61L and LifeAct-mCherry. Region marked by a dashed square surrounding the bead, expanded below at the indicated time points; $t = 0$ min, initial deformation of the cell membrane. TL, transmitted light (FluidFM cantilever) (representative images of GFP, GFP-CDC42-T17N, and GFP-CDC42-WT in fig. S11, F to H). Data are means ± SEM; ****$P < 0.0001$ (E, one-way ANOVA with Dunnett's multiple comparison test). Scale bar, 10 μm (G).

that these Rho GAP domain–containing BAR proteins are likely inactivators of CDC42 in the process studied here. We could assume that upon their depletion, CDC42 remains activated, leading to an increase in actin polymerization or to more stable actin structures.

Next, our focus shifted toward identifying the potential lipid species involved in the mechanism of curvature-mediated actin polymerization. In particular, we explored the role of phosphoinositides (PIs) as they are well-known regulators of actin polymerization at the plasma membrane (32). In this context, $PI(4,5)P_2$ is recognized as the major regulator because of its ability to recruit and activate several components of the actin polymerization machinery at the plasma membrane, including N-WASP (33). Moreover, it was shown that $PI(4,5)P_2$ recruits CDC42 and FNBP1L to lipid bilayers where they promote Arp2/3-dependent actin polymerization in vitro (13, 15). To test the involvement of $PI(4,5)P_2$ in the current process, we used a rapalog-based system, allowing the controlled recruitment of a 5′-phosphatase to the cytosolic leaflet of the plasma membrane and subsequent depletion of $PI(4,5)P_2$ (34). Upon induction of phosphatase recruitment to the cell surface, we observed a complete loss of local actin rings around all nanodeformation sizes, while other actin fibers seemed unaffected (fig. S10, C and D). Of note, the depletion of PI3P species by inhibiting PI3-kinases with wortmannin (35) showed no (or only mild) effect on actin polymerization and CIP4 recruitment (fig. S10, E and F), suggesting that PI3Ps are not involved in the process. Together, these data indicate that curvature-mediated actin polymerization strictly relies on the presence of $PI(4,5)P_2$, but not $PI(3,4,5)P_3$, in the cytosolic leaflet of the plasma membrane.

Local CIP4/CDC42-dependent actin polymerization is dynamic and promoted by plasma membrane curvature

To validate that local CIP4- and CDC42-dependent actin polymerization is promoted by plasma membrane nanoscale curvature, we performed live-cell microscopy experiments to measure protein enrichment in the vicinity of membrane nanodeformations over time. In agreement with the results of a previous study using another strategy to generate nanostructured surfaces (12), we observed that the actin cytoskeleton (labeled with LifeAct) around plasma membrane deformations is dynamic, constantly undergoing rapid assembly and disassembly (movie S2). Pairwise observations of CDC42, CIP4, and actin showed that the three proteins follow very similar dynamics (Fig. 5, A to C, and movies S3 to S5). Of note, PalMyr-mCherry, used here as a plasma membrane marker, did not show any obvious dynamic behavior (Fig. 5D and movie S6). To be more quantitative, we then computed the correlation coefficients between the dynamics of the three proteins, taken by pairs (Fig. 5E). As expected, a positive and significant correlation was observed for the dynamics of CIP4/CDC42, CIP4/LifeAct, and LifeAct/CDC42 couples, while no correlation was observed between the signals of PalMyr-mCherry and LifeAct-GFP, validating the involvement of CIP4 and CDC42 in curvature-induced actin polymerization (Fig. 5E). Similar correlations were observed for the three proteins on 500-nm plasma membrane deformations (fig. S11, A to E, and movies S7 to S9). However, on these larger deformations, a significant correlation was also observed between the dynamics of actin and PalMyr-mCherry (fig. S11, D and E, and movie S10), suggesting that the distribution of the plasma membrane marker itself may be influenced by local actin polymerization. This hypothesis is very likely, as actin polymerization can promote

the formation of lipid rafts in the plasma membrane and local enrichment in lipid-anchored proteins (36–39). Alternatively, actin polymerization may enhance membrane deformations and therefore increase PalMyr-GFP signal artificially.

The deformation of plasma membrane using nanostructured cell culture substrates is a long process, which requires cell adhesion to proceed from 30 min to 2 hours. To grasp the dynamics of CDC42 and local actin polymerization upon acute membrane deformation (within 10 min), we carried out additional experiments on live cells using a FluidFM device coupled to a fast-scanning confocal microscope, already used in a previous study (28). With this unique setup, we were able to induce plasma membrane nanodeformations in a time-, space-, and force-controlled manner while simultaneously imaging protein recruitment in the vicinity of the deformed plasma membrane. Fluorescent 500-nm particles were captured at the tip of the FluidFM probe and pulled toward the apical plasma membrane of cells coexpressing LifeAct-mCherry and different GFP-tagged CDC42 constructs. Upon transient expression of wild-type CDC42, we observed a peak of actin polymerization within 2 min after induction of deformation, followed by a progressive decrease of the signal (Fig. 5F, fig. S11F, and movie S11). A similar behavior was observed in cells expressing free GFP, although the actin signal was lower overall (Fig. 5F, fig. S11G, and movie S12). Expression of the dominant-negative mutant of CDC42 (T17N) completely inhibited actin polymerization around plasma membrane deformations (Fig. 5F, fig. S11H, and movie S13). By contrast, expression of the constitutively active CDC42 mutant (Q61L) led to a continuous increase in actin polymerization throughout the 10-min duration of the experiment (Fig. 5, F and G, and movie S14).

Together, these data show that plasma membrane nanodeformation promotes actin polymerization in a CDC42-dependent manner, possibly through the direct activation of CDC42. Our data also show the highly dynamic nature of this mechanism in cellulo and demonstrate that it can occur at both the basal and apical plasma membranes despite their differences in composition and mechanical properties (40).

Actin polymerization around plasma membrane nanodeformations inhibits IFNγ-R signaling

Extensive literature reports establish that the cortical actin cytoskeleton is an essential regulator of plasma membrane protein organization and function (37, 41). Given the drastic local reorganization of actin observed upon growing cells on nanostructured substrates, one may wonder whether this reorganization could affect signaling pathways. Here, we investigated the signaling of the IFNγ-R, which is one of the major signaling pathways in cells known to be implicated in tumor immune-surveillance and tumor escape, but also in a broad range of inflammatory conditions such as cardiovascular diseases (42, 43). In the current model, IFNγ-R is a complex composed of four chains: two chains IFNγ-R1 and two chains IFNγ-R2. When IFNγ binds to the IFNγ-R complex, a conformational change of the chains occurs, leading to the activation of preassociated Janus-activated tyrosine kinases (JAKs), which triggers the phosphorylation of signal transducer and activator of transcription 1 (STAT1), resulting in its nuclear translocation (44). The main reason why we decided to focus on IFNγ-R signaling is that it is known to be tightly regulated by actin—and lipid—nanodomains: The signaling of a mutant of IFNγ-R displaying additional glycosylations was shown to be strongly inhibited because of its trapping in the cortical

actin meshwork caused by the binding of galectin-1 and galectin-3 (*45*).

First, the subcellular localization of IFNγ-R2 subunit was monitored in HeLa cells expressing IFNγ-R2–GFP seeded on 500-nm nanostructures. The enrichment in IFNγ-R2–GFP around membrane deformations was systematically correlated with actin enrichment (Fig. 6A, white arrowheads). As a corollary, if actin was not enriched, there was no enrichment in IFNγ-R2–GFP (Fig. 6A, purple arrowhead). To be more physiological and avoid potential artifacts due to transient expression, we used Caco-2 cells, which, on the contrary to Hela cells, express IFNγ-R endogenously and respond to IFNγ stimulation. IFNγ-R2 signal was monitored by immunofluorescence after 10 min of stimulation with IFNγ. Although the signal was more discrete/punctuated, we observed endogenous

Fig. 6. Plasma membrane nanodeformations can serve as platforms for IFNγ-R signaling regulation. HeLa (A) or Caco-2 [(B) to (G)] cells. (**A**) Transient expression of IFNγ-R2–GFP (green) without stimulation in cells grown on 500-nm nanostructures (blue). Red signal, actin (phalloidin). Note the co-distribution of IFNγ-R2–GFP and actin signals (white arrowheads), or the simultaneous absence of both signals (purple arrowhead) around nanodeformations. (**B**) Endogenous IFNγ-R2 (green) after 10 min of stimulation with IFNγ in cells grown on 500-nm nanostructures (red). Note the punctate localization of IFNγ-R2 around nanodeformations (yellow arrowheads). (A) and (B) Representative Airyscan images of three independent experiments. Insets, zoom on dashed square regions. (**C** and **D**) STAT1 nuclear translocation experiment upon IFNγ stimulation for indicated times in cells grown on nanostructured substrates. Representative images after 1 hour of stimulation [(C), representative images of all conditions in fig. S12]. Quantifications shown in (D). Two (100 nm) or three (No beads, 300 and 500 nm) independent experiments. (**E**) STAT1 nuclear translocation upon IFNγ stimulation for indicated times in cells grown on 500-nm nanostructures and knocked down for CDC42 or ARPC2. Two independent experiments. (**F** and **G**) Effect of the depletion of ARPC2 or CDC42 on actin polymerization around 500-nm nanostructures. Representative images (F) and quantifications (G). Number of deformations: siCtrl, *n* = 364; siARPC2, *n* = 190; siCDC42, *n* = 289. Single experiment. Data are median with quartiles [(D) and (E)] or means ± SEM. (G); ****P < 0.0001; ***P < 0.001; **P < 0.01; *P < 0.05 [Kruskal-Wallis test with Dunn's multiple comparison [(D) and (E) or one-way ANOVA with Dunnett's multiple comparison (G) tests]. *n*, number of cells [(D) and (E)]. Scale bars, 5 μm (F), 10 μm [(A) and (B)], and 20 μm (C). A.U., arbitrary units.
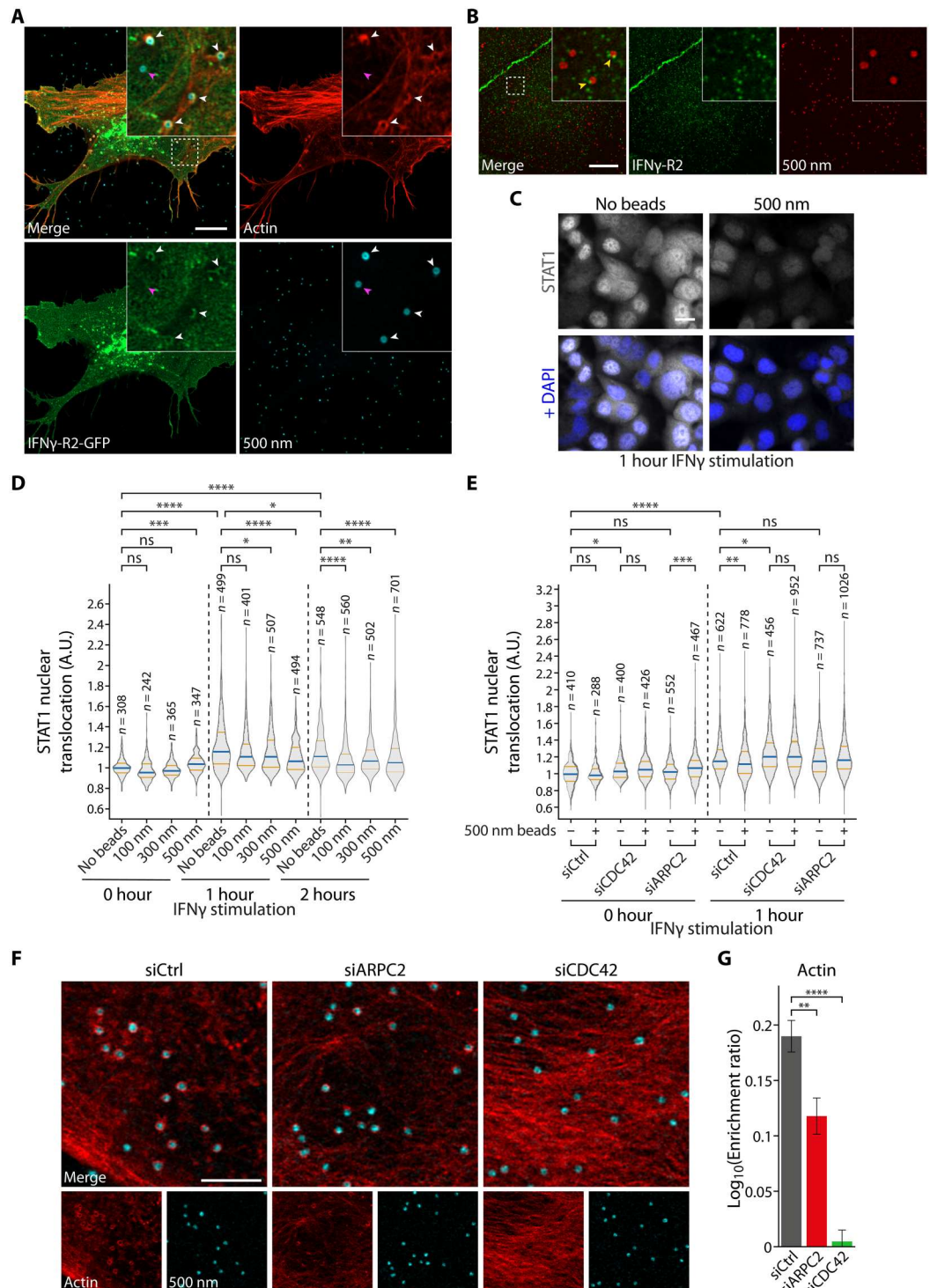
IFNγ-R2 around 500-nm deformations (Fig. 6B, yellow arrowheads).

Consequently, the next logical step was to investigate whether the presence of IFNγ-R in the curvature-induced actin nanodomains would affect its downstream signaling. Therefore, STAT1 nuclear translocation was monitored in Caco-2 cells seeded for 1.5 hours on flat or nanostructured substrates and then treated for the indicated times with IFNγ before fixation (Fig. 6, C and D, and fig. S12). In the absence of IFNγ stimulation, STAT1 nuclear translocation did not occur and its nuclear signal stayed at a basal level in all conditions (Fig. 6D, 0 hours). As expected, STAT1 nuclear translocation increased after IFNγ stimulation in cells grown on surfaces without nanostructures, with a peak at 1 hour (Fig. 6, C and D, 1 and 2 hours). STAT1 nuclear translocation was significantly lower when cells were grown on nanostructures (Fig. 6, C and D). Furthermore, increasing nanostructure size led to a stronger inhibition of IFNγ-STAT1 signaling pathway, with a maximal effect reached with 500-nm nanostructures after 1 hour of treatment with IFNγ (Fig. 6, C and D).

Interestingly, 500-nm deformations induced a dramatic actin cytoskeleton reorganization (Fig. 1J and fig. S7). We hypothesize that these actin-rich nanodomains trap IFNγ-R and prevent its signaling, similarly to what was observed by Blouin *et al.* (*45*). To address this possibility, we monitored STAT1 nuclear translocation upon IFNγ stimulation in Caco-2 cells depleted for CDC42 or Arp2/3 complex subunit 2 (ARPC2) seeded on flat or 500-nm nanostructured substrates (Fig. 6E). Of note, the depletion of either of these two proteins significantly reduced actin ring polymerization around the nanodeformations (Fig. 6, F and G). As previously observed, after 1 hour of IFNγ stimulation, STAT1 nuclear translocation was significantly lower in control cells seeded on 500-nm nanostructures as compared to the flat substrate (Fig. 6E). However, when CDC42 or ARPC2 was depleted, the inhibitory effect of nanostructures on STAT1 nuclear translocation was lost (Fig. 6E). In other words, these observations suggest that the inhibition of IFNγ-R signaling by the nanostructures is dependent on the actin cytoskeleton reorganization induced by the plasma membrane nanodeformations. The reduction of actin polymerization around membrane deformations was thus able to restore IFNγ-R signaling. Together, these results highlight that IFNγ-R is localized in actin nanodomains formed around plasma membrane deformations and that its downstream IFNγ-induced JAK/STAT1 signaling is severely impaired by the actin nanodomains forming around 500-nm nanostructures.

DISCUSSION

Our screening dissociated the two functions of BAR domain proteins—as membrane curvature sensors versus inducers—to solely study their ability to sense/bind to preexisting deformations in vivo. We found that BAR proteins from all subfamilies—except for PX-BAR—were able to bind membrane deformations of every tested size. Hence, there seems to be no apparent correlation between the intrinsic curvature radius of BAR proteins and their affinity for a particular membrane deformation size. In particular, both N-BAR and F-BAR proteins—usually thought to bind highly or shallowly curved membrane, respectively—were recruited on all deformation sizes. Thus, the classical view suggesting that BAR domain protein subfamily classification depicts their ability to

bind/induce distinct membrane curvature ranges is challenged by our results (*18–20*). Their curvature range affinity seems more protein specific than family/intrinsic curvature radius dependent. Unexpectedly, amphiphysin, which was previously shown to be membrane curvature sensitive, was not enriched at all in our screen (*14*). This could be due to differences in experimental setups such as the nanostructure size, geometry, or the cell type used. Amphiphysin could possibly be in an autoinhibited state—due to its SH3 domains folding onto the BAR domain—and thus is unable to bind membrane deformations (*46*). Furthermore, multiple proteins bound to a range of curvature radii, while others were restricted to a more specific curvature radius. A very likely explanation for this observation resides in the flexibility and plasticity of some BAR oligomer scaffolds to adapt to broad membrane curvature ranges as shown for some F-BAR proteins (*47, 48*). However, the extent of this plasticity remains to be explored. While the overall membrane curvature generated by our nanostructures is positive, a saddle-shaped curvature is observed at the connecting plane between a nanoparticle and the flat substrate. At this location, both a positive and a negative membrane curvature coexist. Some BAR domain proteins could be favorably recruited to this saddle point, such as I-BARs, as demonstrated with MIM. Further studies, focusing on the precise localization of BAR domain proteins at the nanometer scale in three dimensions (3D), will be necessary to assess the significance of the membrane's saddle shape.

Our screening results showed that a unique set of BAR domain proteins bound to each size of deformation. These unique sets of BAR proteins would allow cells to adapt and react in a specific way depending on the nanogeometry of their plasma membrane. Distinct processes might be regulated locally, which could be of importance for mechanotransduction. Some pathways could be favored or coupled together to elicit a variety of responses depending on the cellular context and the nature of the cells' mechanical environment. In this work, we mostly focused on curvature-mediated actin polymerization through TOCA proteins, but other BAR domain proteins showed unique patterns or dynamics. In particular, EndophilinA3, which is involved in clathrin-independent endocytosis, showed intriguing dynamics around membrane deformations. Membrane curvature might promote its assembly on plasma membrane to facilitate endocytosis. This coupling between plasma membrane curvature and endocytosis dynamics was previously demonstrated for clathrin-mediated endocytosis and proposed for clathrin-independent pathways (*10, 11, 49, 50*). These curved membrane regions could therefore be hotspots for various endocytic pathways because of the possible reduction of membrane bending energy. We did not observe the recruitment of other EndophilinA isoforms (A1 and A2) to plasma membrane deformations in our setup. Despite their high sequence similarity, they were previously shown to localize in different plasma membrane areas and to control the endocytosis of distinct subsets of cargoes (*28*). However, the origin of these differences remains unknown. Nevertheless, our results further underline the functional differences between EndophilinA isoforms. Sensitivity to various types of membrane curvature might play a role in the specific localization of each isoform and their corresponding endocytic mechanism within distinct plasma membrane regions.

In our model, TOCA proteins are necessary for actin polymerization to occur only on 100-nm membrane deformations. Other BAR domain proteins could fulfil their role regarding actin

polymerization on bigger deformations. Among them, Nostrin and SNX9 are good candidates. Nostrin, which displays the same domain organization as TOCA proteins, was recruited on 500-nm deformations and also influences actin dynamics (51). On the other hand, SNX9 was shown to be able to replace FNBP1L and to recruit N-WASP to mediate actin polymerization when PI3P is present in curved supported lipid bilayers instead of PI(4,5)P2 (15). However, SNX9 was only recruited at a low level to membrane deformations in our screening. Unlike other BAR domain proteins, its recruitment might be short-lived or restricted to only a subpopulation of membrane deformations. Therefore, additional research to observe the dynamics of Nostrin, SNX9, and actin cytoskeleton on membrane deformations is needed to assess the potential involvement of these proteins in the current mechanism.

While the TOCA subfamily has been previously involved in curvature-mediated actin polymerization (12), our study is the first to connect the Rho GTPase CDC42 to this mechanism in cellulo. Specifically, our results suggest that the activity of CDC42, an early player involved in actin polymerization, might be curvature dependent. Although we did not provide any direct demonstration, several indirect observations in our study argue in favor of this hypothesis. We observed changes in curvature-mediated actin polymerization by modulating CDC42 activity using constitutively active and dominant-negative mutants, inhibitors, and more importantly by the transient expression of Rho GAP proteins, which are well known to target CDC42. We showed that some Rho GAP–containing BAR domain proteins—Nadrin2, Oligophrenin, and srGAP3—decreased actin polymerization around plasma membrane nanodeformations, most likely by deactivating CDC42 (52–54). This could possibly explain the transient nature of actin rings. However, we have not yet identified Rho guanine nucleotide-exchange factor (GEF) candidates, which could activate CDC42 in the first place. Unexpectedly, there are very few Rho GEF proteins among the BAR superfamily. Additional experiments will thus be necessary to monitor directly CDC42 activity, to establish whether it is regulated by membrane curvature itself, and to identify the GEFs involved in the mechanism.

In addition, our RNA interference experiments showed that CDC42—and not Rac1—is necessary for curvature-mediated actin polymerization to occur, which was previously only demonstrated in in vitro studies on liposomes, and flat or curved supported lipid bilayers (13, 15, 55). The findings reported by Gallop et al. (15) using an in vitro model system share multiple similarities with our own observations, such as the involvement of CDC42, FNBP1L, and PI(4,5)P2 in actin polymerization on curved membranes. Similarly, Takano et al. (55) demonstrated CDC42- and FNBP1L-mediated actin polymerization on liposomes, but in their case, it was independent of PI(4,5)P2. After activation of CDC42 and recruitment of TOCAs to membrane deformations, it seems that actin polymerization occurs through Arp2/3 complex activation as we observed that its depletion inhibits local polymerization. N-WASP is also likely to be involved in the process according to previous studies (12, 15, 55, 56).

The large plasma membrane nanodomains described in our study, induced by 300- and 500-nm nanostructures, led to a cellular response independently of clathrin-mediated endocytic machinery. By contrast, clathrin machinery seemed to play a more prominent role in the case of small plasma membrane nanodomains induced by 100-nm nanostructures, as shown by the effect of AP2 complex depletion on actin polymerization. However, we did not observe any specific enrichment of clathrin around the nanostructures, whatever their size. This questions the effective role of clathrin-mediated endocytic machinery around smaller plasma membrane deformations, which might be indirect. Future investigations will be necessary to clarify this point. Nevertheless, our plasma membrane nanodomains are reminiscent of early-stage FEME-like endocytic pits. In FEME, locally activated CDC42 recruits CIP4 and FBP17 to prime the membrane for endocytosis before being inactivated because of Rho GAP–containing BAR domain proteins (Nadrin1, SH3BP1, and Oligophrenin) in the absence of receptor activation or stabilization (21). Most of these various characteristic molecular actors are involved in the membrane nanodomains we described here. This opens up the exciting possibility of the existence of a frustrated clathrin-independent endocytosis, similar to the previously documented phenomenon of frustrated clathrin-mediated endocytosis (22, 23). While further research is required to support this hypothesis, these frustrated structures could also serve as signaling platforms promoting the accumulation of receptors and adaptor proteins or acting as a scaffold for the organization of the actin cytoskeleton.

In particular, previous studies have already reported the formation of actin structures on topography-induced membrane deformations, connecting them to various cellular functions such as adhesion, migration, or endocytosis (10, 12, 57, 58). Here, we propose that these structures can also act as platforms regulating cell surface receptor signaling. We showed that IFNγ-R colocalizes with actin-rich domains forming around membrane nanodeformations and that its signaling is significantly impaired by their presence. Blouin et al. (45) showed previously that IFNγ-R signaling was inhibited when the receptor is trapped in the cortical actin meshwork. We propose that a similar regulation occurs on topography-induced plasma membrane deformations, which enhance the formation of numerous and dense actin structures (i.e., actin rings) throughout the membrane. This could increase the probability for IFNγ-R of being trapped, preventing its signaling. In support of this hypothesis, we observed that the disruption of actin rings alleviates the inhibitory effect on IFNγ-R signaling. In addition, it is tempting to establish a direct conceptual analogy between the FEME-like structures described in our study and frustrated clathrin-mediated endocytosis described by other groups, where clathrin plaques were shown to act as platforms regulating receptor signaling (in particular, for epidermal growth factor receptor) (22–24). Although we cannot rule out that nanostructure surface properties affect IFNγ-R signaling, it seems unlikely as surface chemistry and stiffness are homogeneous in our setup. However, additional investigations are necessary to characterize IFNγ-R dynamics within these topography-induced actin nanodomains. It will also be of great interest to explore whether other receptors are trapped in these actin structures and whether their signaling is also affected.

In conclusion, our study sheds light on the poorly explored connection between plasma membrane nanogeometry and signal transduction mechanisms. We deciphered a mechanotransduction pathway induced by membrane nanodeformation, which involves the BAR domain protein CIP4, the Rho GTPase CDC42, and actin cytoskeleton. Furthermore, actin cytoskeleton remodeling triggered by substrate nanotopography is capable of tuning type II IFN signaling. These findings may be key to understanding how substrate nanotopography influences cell behavior in biological

contexts as diverse as development, cancer progression, or for the design of biocompatible materials, to cite only a few examples.

MATERIALS AND METHODS
Antibodies and other reagents
The following antibodies were purchased from the indicated suppliers: mouse monoclonal anti-CIP4 (Santa Cruz Biotechnology, sc-135868, 1:500 for immunofluorescence and 1:1000 for Western blot), mouse monoclonal anti-CDC42 (Cytoskeleton Inc., ACD03, 1:250 for Western blot), mouse monoclonal anti-Rac1 (Merck Millipore, 05-389, 1:1000 for Western blot), mouse monoclonal anti–clathrin heavy chain (BD Biosciences, 610500, 1:100 for immunofluorescence and 1:5000 for Western blot), mouse monoclonal anti–α-tubulin (Sigma-Aldrich, T5168, 1:5000 for Western blot), mouse monoclonal anti–β-actin (Santa Cruz Biotechnology, sc-47778, 1:1000 for Western blot), rabbit polyclonal anti–IFNγ-R2 (Proteintech, 10266-1-AP, 1:200 for immunofluorescence), rabbit monoclonal anti-STAT1 (D1K9Y) (Cell Signaling Technology, 14994, 1:300 for immunofluorescence), rabbit monoclonal anti-AP2M1 (Abcam, ab75995, 1:1000 for Western blot), secondary antibodies conjugated to Alexa Fluor 488 or 647 (Thermo Fisher Scientific, 1:250 for immunofluorescence), anti-mouse secondary antibody conjugated to STAR ORANGE (Abberior, STORANGE-1001, 1:200 for immunofluorescence), and anti-mouse and anti-rabbit secondary antibodies conjugated to horseradish peroxidase (Sigma-Aldrich and Dako, respectively, 1:5000 for Western blot). The rabbit polyclonal anti-FBP17 (1:1000 for Western blot) was a gift from P. De Camilli (New Haven, USA), and the mouse monoclonal anti-FNBP1L (1:25 for Western blot) was a gift from E. Frittoli (Milan, Italy). Phalloidin conjugated to Alexa Fluor 488 (A12379) or Alexa Fluor 633 (A22284), Alexa Fluor 488 N-hydroxysuccinimide (NHS) ester (A20000), Alexa Fluor 555 NHS ester (A20009), rapamycin (PHZ1235), and PageRuler Prestained Protein Ladder (26617) were purchased from Thermo Fisher Scientific. Phalloidin conjugated to STAR RED (STRED-0100) was purchased from Abberior. ATTO 390 (AD 390) and ATTO 647N (AD 647N) were purchased from ATTO-TEC. Phalloidin conjugated to iFluor 555 (ab176756) was purchased from Abcam. PAH solution (479144) and ML141 (SML0407) were purchased from Sigma-Aldrich. Silica colloids of 500 nm (24323-15), 300 nm (24321-15), and 100 nm (24041-10) were purchased from Polysciences. Of note, the diameter of silica colloids has a coefficient of variation of 10 to 15%. Wortmannin (HY-10197) was purchased from MedChemExpress. Human IFNγ was purchased from Imukin.

Synthesis of nanostructured substrates
Fluorescent silica colloid synthesis
Spherical silica colloids of 500 nm (0.075 wt %) were first coated with 0.025 wt % PAH solution for 30 min at room temperature. They were then washed six times by centrifugation at 10,000g followed by resuspension in water. Next, PAH-coated colloids were fluorescently labeled with NHS ester–conjugated dyes (10 μg ml^{-1}) (ATTO 390, Alexa Fluor 488, Alexa Fluor 555, or ATTO 647N) for 1 hour at room temperature in water. Colloids were washed six more times by centrifugation at 21,000g followed by resuspension in water. The fluorescent colloid suspension was then stored at 4°C protected from any light until further use. For colloids of 300 and 100 nm, the procedure was the same except that they

were coated with 0.05 wt % PAH, and colloids of 100 nm were labeled with of fluorescent dyes (20 μg ml^{-1}).
Fluorescent silica colloid adsorption
Fluorescent silica colloids were diluted in water to 0.024 wt % for 500 nm, 0.0045 wt % for 300 nm, and 0.0006 wt % for 100 nm and transferred to a 10-mm optical glass fluorescent cuvette. Two coverslips (WillCo Wells, 12 mm in diameter) were pressed together, placed vertically in the cuvette, and incubated for 2 hours in the dark at room temperature. After incubation, water was slowly added at the top of the cuvette and the same volume was removed at the bottom. This washing procedure was repeated six times, with the last three being carried out with 100% isopropanol (VWR). Coverslips were then separated and individually dipped in isopropanol before being placed in four-well plates, nanostructures facing up. Coverslips were left to dry and kept in the dark at room temperature until further use. For live cell imaging, nanostructures were created on coverslips of 35 mm in diameter in the same way and assembled into dishes using WillCo-dishKIT "Do-It-Yourself."
Collagen coating
Dry nanostructured coverslips were incubated with collagen (100 μg ml^{-1}) (Bornstein and Traub Type I, Sigma-Aldrich, C8919) in phosphate-buffered saline (PBS; Sigma-Aldrich) for 1 hour in the dark at room temperature. Coverslips were then washed twice with PBS and twice with ethanol 70% (VWR). The collagen-coated coverslips were kept up to 48 hours before cell seeding.
Surface characterization
Collagen-coated nanostructured substrates were sputter-coated with gold before imaging with a JEOL 7600F scanning electron microscope.

Cell culture
HeLa [human cervix adenocarcinoma, American Type Culture Collection (ATCC) CCL-2] were grown at 37°C under 5% CO$_2$ in Dulbecco's Modified Eagle Medium (DMEM) high-glucose GlutaMAX (Gibco, 61965-059) supplemented with 10% fetal bovine serum (FBS), penicillin (100 U ml^{-1}), streptomycin (100 μg ml^{-1}), and 1 mM pyruvate. Caco-2 (colorectal adenocarcinoma, ATCC HTB-37) were grown at 37°C under 5% CO$_2$ in DMEM low glucose pyruvate (Gibco, 31885-023) supplemented with 10% FBS, penicillin (100 U ml^{-1}), and streptomycin (100 μg ml^{-1}).

DNA constructs and transfection
For all DNA transfection experiments except for IFNγ-R2–eGFP, plasmids were transfected with FuGene HD (Promega, E2311) in HeLa cells according to the manufacturer's instructions. Cells were used for experiments 16 to 24 hours after transfection. IFNγ-R2–eGFP (enhanced GFP) plasmid was transfected in HeLa or Caco-2 cells with X-tremeGENE HP DNA transfection reagent (Roche, 6366236001) according to the manufacturer's instructions for 24 hours and with the following ratio: 1 μg of DNA per 2 μl of transfection reagent. All the plasmid used can be found in Tables 1 and 2.

RNA interference
Small interfering RNAs (siRNAs) used in this study were purchased from Qiagen or Dharmacon and transfected with HiPerFect (Qiagen, 301704) according to the manufacturer's instructions. Experiments were always performed 72 hours after siRNA transfection, where protein depletion efficiency was maximal as shown by

Table 1. Plasmids containing BAR domain protein sequences used in this study.

Protein	Species	Backbone	Promoter	Tag	Source	Additional information
Arfaptin2	Human	pCI	CMV	C-ter GFP	H. T. McMahon (Cambridge, UK)	BAR domain only
FAM92B	Human	pCI	CMV	C-ter GFP	H. T. McMahon (Cambridge, UK)	
ICA1L	Human	pCI	CMV	C-ter GFP	H. T. McMahon (Cambridge, UK)	BAR domain only
ICA69	Human	pCI	CMV	C-ter GFP	H. T. McMahon (Cambridge, UK)	BAR domain only
PICK1	Rat	pEYFP-C1	CMV	N-ter YFP	Madsen *et al.* (*61*)	
Amphiphysin	Human	pEGFP-C1	CMV	N-ter GFP	Yamada *et al.* (*62*)	
Bin1	Human	pEGFP-C1	CMV	N-ter GFP	Lee *et al.* (*63*)	
Bin2	Human	pEGFP-N3	CMV	C-ter GFP	M. J. Sanchez-Barrena (Madrid, Spain)	
Bin3	Mouse	pEGFP-N1	CMV	C-ter GFP	F. Tyckaert (Louvain-la-Neuve, Belgium)	
Endophilin A1	Human	pcDNA3	CMV	C-ter GFP	H. T. McMahon (Cambridge, UK)	
Endophilin A2	Rat	pEGFP-N1	CMV	C-ter GFP	P. De Camilli (New Haven, USA)	
Endophilin A3	Human	pcDNA3	CMV	C-ter GFP	H. T. McMahon (Cambridge, UK)	
Endophilin B1	Human	pEYFP-N1	CMV	C-ter YFP	Karbowski *et al.* (*64*)	
Endophilin B2	Human	pCI	CMV	C-ter GFP	H. T. McMahon (Cambridge, UK)	BAR domain only
Nadrin1	Human	pEYFP-N3	CMV	C-ter YFP	I. Begemann (Münster, Germany)	
Nadrin2	Human	pEYFP-N3	CMV	C-ter YFP	I. Begemann (Münster, Germany)	BAR domain only
SH3BP1	Human	pmCherry-C1	CMV	N-ter mCherry	M. C. Parrini (Paris, France)	
ACAP1	Human	pEGFP-C1	CMV	N-ter GFP	Li *et al.* (*65*)	
ACAP2	Mouse	pEGFP-C1	CMV	N-ter GFP	M. Fukuda (Sendai, Japan)	
ACAP3	Human	pCI	CMV	C-ter GFP	H. T. McMahon (Cambridge, UK)	BAR domain only
APPL1	Mouse	pmCherry-C1	CMV	N-ter mCherry	Addgene #27683	
ASAP2	Human	pCI	CMV	C-ter GFP	H. T. McMahon (Cambridge, UK)	BAR domain only
Graf1	Human	pEGFP-C3	CMV	N-ter GFP	R. Lundmark (Umeå, Sweden)	
Graf2	Human	pCI	CMV	C-ter GFP	H. T. McMahon (Cambridge, UK)	BAR domain only
Oligophrenin1	Human	pEGFP-N3	CMV	C-ter GFP	L. Van Aelst (New York, USA)	
SNX1	Human	pEGFP-C1	CMV	N-ter GFP	P. Cullen (Bristol, UK)	
SNX2	Human	pEGFP-C1	CMV	N-ter GFP	P. Cullen (Bristol, UK)	
SNX4	Human	pEGFP-C1	CMV	N-ter GFP	P. Cullen (Bristol, UK)	
SNX5	Human	pEGFP-C1	CMV	N-ter GFP	P. Gleeson (Melbourne, Australia)	
SNX6	Human	pEGFP-C1	CMV	N-ter GFP	P. Cullen (Bristol, UK)	
SNX7	Human	pEGFP-C1	CMV	N-ter GFP	Pete Cullen (Bristol, UK)	
SNX8	Human	pEGFP-C1	CMV	N-ter GFP	Pete Cullen (Bristol, UK)	
SNX9	Mouse	pmCherry-C1	CMV	N-ter mCherry	Addgene #27678	
SNX18	Human	pDEST	CMV	N-ter GFP	A. Simonsen (Oslo, Norway)	
SNX30	Human	pEGFP-C1	CMV	N-ter GFP	P. Cullen (Bristol, UK)	
SNX32	Human	pEGFP-C2	CMV	N-ter GFP	P. Cullen (Bristol, UK)	
SNX33	Human	pEGFP-C2	CMV	N-ter GFP	P. Cullen (Bristol, UK)	
ARHGAP4	Human	pEGFP-C1	CMV	N-ter GFP	K. Gould (Nashville, USA)	
ARHGAP4	Human	pEGFP-C1	CMV	N-ter GFP	K. Gould (Nashville, USA)	BAR domain only
ARHGAP29	Human	pcDNA3	CMV	N-ter YFP	J. Bos (Utrecht, The Netherlands)	
CIP4	Mouse	pmCherry-C1	CMV	N-ter mCherry	Addgene #27685	
CIP4 F-BAR	Mouse	pmCherry-C1	CMV	N-ter mCherry	H. T. McMahon (Cambridge, UK)	a.a. 1–274
CIP4 F-BAR+	Mouse	pmCherry-C1	CMV	N-ter mCherry	H. T. McMahon (Cambridge, UK)	a.a. 1–337
CIP4 ΔSH3	Mouse	pmCherry-C1	CMV	N-ter mCherry	H. T. McMahon (Cambridge, UK)	a.a. 1–427
CIP4 ΔREM1	Mouse	pmCherry-C1	CMV	N-ter mCherry	H. T. McMahon (Cambridge, UK)	a.a. 1–273 + 428–547

continued on next page

Protein	Species	Backbone	Promoter	Tag	Source	Additional information
CIP4 ΔBasic	Mouse	pmCherry-C1	CMV	N-ter mCherry	H. T. McMahon (Cambridge, UK)	a.a. 1–308 + 333–547
FBP17	Human	pmCherry-C1	CMV	N-ter mCherry	Addgene #27688	
FCHo1	Mouse	pmCherry-C1	CMV	N-ter mCherry	Addgene #27690	
FCHo2	Mouse	pmCherry-C1	CMV	N-ter mCherry	Addgene #27686	
FCHSD1	Mouse	pEGFP-C2	CMV	N-ter GFP	Z. Xu (Shandong, China)	
FCHSD2	Mouse	pEGFP-C2	CMV	N-ter GFP	Z. Xu (Shandong, China)	
Fer	Human	pEGFP-C1	CMV	N-ter GFP	K. Gould (Nashville, USA)	
Fer	Human	pEGFP-C1	CMV	N-ter GFP	K. Gould (Nashville, USA)	BAR domain only
Fes	Human	pEGFP-C1	CMV	N-ter GFP	K. Gould (Nashville, USA)	BAR domain only
FNBP1L	Human	pEGFP-C1	CMV	N-ter GFP	P. De Camilli (New Haven, USA)	
GAS7	Human	pEGFP-N1	CMV	C-ter GFP	C. C.K. Chao (Taoyuan, Taiwan)	
GMIP	Mouse	pEGFP-N1	CMV	C-ter GFP	K. Sawamoto (Nagoya, Japan)	
HMHA1	Human	pEGFP-C3	CMV	N-ter GFP	P. Hordijk (Amsterdam, The Netherlands)	
Nostrin	Human	pEGFP-C1	CMV	N-ter GFP	K. Gould (Nashville, USA)	BAR domain only
PACSIN1	Mouse	pEGFP-N3	CMV	C-ter GFP	S. Suetsugu (Ikoma, Japan)	
PACSIN2	Mouse	pmCherry-C1	CMV	N-ter mCherry	Addgene #27681	
PACSIN3	Mouse	pEGFP-N3	CMV	C-ter GFP	S. Suetsugu (Ikoma, Japan)	
PSTPIP1	Human	pEGFP-C2	CMV	N-ter GFP	D. Gumucio (Ann Arbor, USA)	
PSTPIP2	Human	pCI	CMV	C-ter GFP	H. T. McMahon (Cambridge, UK)	
srGAP1	Human	pCAG-EGFP	CAG	N-ter GFP	F. Polleux (New York, USA)	
srGAP1	Human	pCAG-EGFP	CAG	N-ter GFP	F. Polleux (New York, USA)	BAR domain only
srGAP2	Human	pCAG-EGFP	CAG	N-ter GFP	F. Polleux (New York, USA)	
srGAP2	Mouse	pCAG-mRFP	CAG	N-ter RFP	F. Polleux (New York, USA)	BAR domain only
srGAP3	Human	pCAG-EGFP	CAG	N-ter GFP	F. Polleux (New York, USA)	
srGAP3	Human	pCAG-EGFP	CAG	N-ter GFP	F. Polleux (New York, USA)	BAR domain only
IRSp53	Human	pCI	CMV	C-ter GFP	H. T. McMahon (Cambridge, UK)	BAR domain only
IRTKS	Human	pCI	CMV	C-ter GFP	H. T. McMahon (Cambridge, UK)	BAR domain only
MIM	Human	pCI	CMV	C-ter GFP	H. T. McMahon (Cambridge, UK)	BAR domain only
Pinkbar	Human	pCI	CMV	C-ter GFP	H. T. McMahon (Cambridge, UK)	BAR domain only

immunoblotting analysis with specific antibodies. AllStars Negative Control siRNA (Qiagen, 1027281) served as a reference point. Depletion of each protein was achieved using one to four different sequences (Table 3) used as a pool at a total final concentration of 40 nM. To deplete CIP4, FBP17, and FNBP1L concomitantly, two siRNA sequences per protein were used at a total final concentration of 40 nM.

Focused ion beam–scanning electron microscopy
HeLa cells seeded on collagen-coated nanostructured substrates were rinsed once with PBS and fixed for 3 hours on ice using 2.5% glutaraldehyde/2% paraformaldehyde (PFA) in buffer A (0.15 M cacodylate and 2 mM CaCl₂). Then, the cells were extensively washed on ice in buffer A, then incubated for 1 hour on ice in 2% osmium tetroxide and 1.5% potassium Ferro cyanide in buffer A, and, finally, rinsed five times for 3 min in distilled water at room temperature. Cells were then incubated for 20 min at room temperature in 0.1 M thiocarbohydrazide, which had been passed through a 0.22-μm filter, and extensively washed with water. Samples were incubated overnight at 4°C protected from light in 1% uranyl-

acetate, washed in water, further incubated in 20 mM Pb aspartame for 30 min at 60°C, and, finally, washed in water after this last contrasting step. Samples were dehydrated in a graded series ethanol, embedded in hard Epon, and incubated for 60 hours at 45°C and then for 60 hours at 60°C. A small block was cut using an electric saw, and the coverslip was removed from the resin by thermal shock using liquid nitrogen. Last, the block was mounted on a pin, coated with gold, and inserted into the chamber of the HELIOS 660 Nanolab DualBeam SEM/FIB microscope (FEI Co., Eindhoven, The Netherlands). Regions of interest (ROIs) were prepared using FIB, and ROI was set to be approximatively 20-μm wide. For imaging, electrons were detected using an Elstar In-Column secondary electrons detector. During the acquisition process, the thickness of the FIB slice between each image acquisition was 10 nm. Bead and membrane segmentations were obtained using LimeSeg plugin of ImageJ (59).

BAR domain protein screening
HeLa cells transiently expressing the plasmids (Tables 1 and 2) were harvested and then seeded on collagen-coated nanostructured

Table 2. Other plasmids used in this study.

Protein name	Species	Backbone	Source
PalMyr-GFP	–	pEGFP-C1	D. Gehrlich (Vienna, Austria)
PalMyr-mCherry	–	pmCherry-C1	G. Boncompain (Paris, France)
LifeAct-GFP	–	pIRES	P. Chavrier (Paris, France)
LifeAct-mCherry	–	pIRES	P. Chavrier (Paris, France)
GFP	–	pEGFP-C1	Clontech (discontinued)
mCherry	–	pmCherry-C1	Clontech
CDC42-WT	Mouse	pEGFP-C1	A. Ridley (London, UK)
CDC42-T17N	Human	pEGFP-C1	F. Niedergang (Paris, France)
CDC42-Q61L	Human	pcDNA3	Addgene #12600
Rac1-WT	Human	pEGFP-C1	F. Niedergang (Paris, France)
PM-FRB-GFP	–	pEGFP-N1	(34) provided by V. Haucke (Berlin, Germany)
mRFP-FKBP12-5'Ptase	–	pmRFP-C1	(34) provided by V. Haucke (Berlin, Germany)
IFNγ-R2	Human	pcDNA3.1 V5/His	C. Blouin (Paris, France)

substrates. They were cultured for 1 hour at 37°C before fixation and mounting.

Dose-dependent inhibition of CDC42
Cells were preincubated for 1 hour in medium containing 1% dimethyl sulfoxide (DMSO; Sigma-Aldrich) (control condition) and 20, 50, or 100 μM ML141 in DMSO. Cells were then harvested and seeded on collagen-coated nanostructured substrates under the same ML141 concentrations for 1 hour before fixation and labeling.

PI level manipulation
For the depletion of PI3 species, cells were seeded on collagen-coated nanostructured substrates, and either 1 μM wortmannin in DMSO or 0.1% DMSO (control condition) was immediately added to the medium. Cells were cultured for 1 hour on the substrates before fixation and labeling.

For the rapalog-based system used to deplete $PI(4,5)P_2$, cells previously transfected with both PM-FRB-GFP and mRFP-FKBP12-5'Ptase were seeded on collagen-coated nanostructured substrates and cultured for 50 min. Next, 20 nM rapamycin in DMSO or 0.2% DMSO (control condition) was added to the medium for 10 min before cell fixation and labeling.

STAT1 nuclear translocation assay
Caco-2 cells were seeded at 80% confluency for 1.5 hours in complete medium on collagen-coated nanostructured substrates. Cells were gently washed twice with PBS and then starved for 20 min in medium without serum to avoid any signaling background.

Next, cells were stimulated or not with IFNγ (1000 U ml^{-1}) for 1 or 2 hours before fixation and labeling.

Sample preparation for fluorescence microscopy
For all experiments except STAT1 nuclear translocation assay, cells were fixed with 4% PFA (Electron Microscopy Sciences, 15710) at 37°C for 15 min before quenching with 50 mM NH$_4$Cl for at least 15 min. If needed, cells were then permeabilized with saponin [0.02% saponin (Sigma-Aldrich, 47036) and 0.2% bovine serum albumin (BSA; Sigma-Aldrich, A9647) in PBS] for 30 min. Cells were then incubated with primary and secondary antibodies and/or phalloidin for 50 min in saponin and mounted in Fluoromount G (Invitrogen).

For STAT1 nuclear translocation assay, cells were fixed with 4% PFA for 10 min at room temperature, quenched in 50 mM NH$_4$Cl for 10 min, and permeabilized with 0.1% Triton X-100 in 0.2% BSA in PBS for 10 min. After blocking with 0.2% BSA in PBS for 20 min, cells were incubated with primary anti-STAT1 antibody for 45 min at room temperature followed by secondary antibody labeling. To finish, coverslips were mounted in Fluoromount G (eBioscience) with 4′,6-diamidino-2-phenylindole (DAPI) (2 μg ml^{-1}, Sigma-Aldrich) to label nuclei.

Light microscopy
Fixed samples were imaged with a 34-channel Zeiss LSM 710 or LSM 900 confocal microscope equipped with an Airyscan detector and with a Plan Apo 63× numerical aperture (NA) 1.4 oil immersion objective. Wide-field images were acquired on a Zeiss LSM 900 microscope equipped with an sCMOS Prime 95B camera and a Plan Apo 40× NA 1.3 oil immersion objective.

2D STED super-resolution imaging was performed with a STEDYCON (Abberior Instruments GmbH) mounted on an upright microscope base (Zeiss AxioImager Z.2) equipped with a Zeiss Plan Apochromat 100×, NA 1.4 oil immersion objective actuated by a z-piezo with 100-μm range (Physik Instruments). In STED mode, 100% of a maximum nominal STED laser output of 1.25 W (775 nm) was used, leading to a theoretical spatial resolution of 35 to 40 nm. STAR RED and STAR ORANGE were excited by pulsed laser sources at 640 and 561 nm, respectively. Pinhole size was 1.13 Airy units at 650 nm. Gated detection in single-photon counting mode was performed using Avalanche photodetectors.

For live-cell imaging, the previously described Zeiss LSM microscopes were equipped with stage-top incubation chambers, allowing temperature and CO$_2$ control. Cells were imaged 30 min after seeding on nanostructured substrates. Several time series of 30 min were then recorded over the course of 2 hours. Observations were made at 37°C and 5% CO$_2$.

Correlative FluidFM/fast-scanning confocal microscopy
For the dynamic study of actin recruitment upon defined membrane deformation, we used a combined instrument, made up of a FluidFM setup (Cytosurge) coupled to a Bruker Resolve AFM and to a Zeiss LSM980 fast-scanning confocal microscope equipped with a Plan Apo 63× NA 1.4 water immersion objective. HeLa cells previously seeded in 40-mm glass-bottom dishes (WillCo-dish) were transfected with the required plasmids 16 to 24 hours before the experiment. Culture media were refreshed just before starting the experiment. Observations were made at 37°C and 5% CO$_2$.

A suspension of fluorescent silica colloids labeled with ATTO 647N was placed on a glass-bottom petri dish and imaged with

Table 3. siRNAs used in this study.

Target protein	Supplier	Reference	Sequence (5′- 3′)
CIP4	Qiagen	SI00061523	TTGGAAGAACGCAGTCGTGAA
	Qiagen	SI00061530	CACCATTGATGTACATACTCA
FBP17	Qiagen	SI03019128	AAGCAGCTTGAATCTAGTAAA
	Qiagen	SI04285652	AACTTTCACGATGGCCGTAAA
FNBP1L	Qiagen	SI04146198	ATGAATAACATTGACCGCCTA
	Qiagen	SI04175500	TTGAATCTCGTTACAGGGTTA
CDC42	Qiagen	SI04381671	GGCGATGGTGCTGTTGGTAAA
Rac1	Qiagen	SI03065531	CAGCACGTGTTCCCGACATAA
	Qiagen	SI03040884	ACGAAGTGGAGATTTACACTA
Clathrin heavy chain	Qiagen	SI00299873	AAGGAGAGTCTCAGCCAGTGA
	Qiagen	SI00299880	TAATCCAATTCGAAGACCAAT
	Qiagen	SI04152372	AAGGGCTAACGTCCCAAATAA
	Qiagen	SI04190417	CCCTGAGTGGTTAGTCAACTA
µ2-adaptin	Qiagen	SI02777355	TGCCATCGTGTGGAAGATCAA
Nadrin1	Qiagen	SI02780449	AAGCAGTGCGTTAACTATCTA
	Qiagen	SI03061282	CACGGTGCGGTCAATATGCCA
Nadrin2	Qiagen	SI04216527	CAGCGTCGCCACGGATAATAT
	Qiagen	SI04230198	CAAACGCTAATAGAAGTGCAA
Oligophrenin1	Qiagen	SI00039235	GCCCTTGGACTTAACACTGAA
	Qiagen	SI00039242	TAGGGCCACAGTCCCTTTAAA
srGAP1	Qiagen	SI00733026	CCCGCTCACAGTATAATACTA
	Qiagen	SI03195234	CGGAACGAATATCTCCTAACA
srGAP2	Qiagen	SI03163447	CACGAGCGATGACGAATGTGA
	Qiagen	SI04191292	CAGAACGACCATGACATGGAT
srGAP3	Qiagen	SI03160395	CACCAACGCAGCTATAAGCAA
	Qiagen	SI04162480	CCCGCATATCGTCACTGGAAA
ARPC2	Dharmacon	J-012081-05	CCATGTATGTTGAGTCTAA
	Dharmacon	J-012081-06	GCTCTAAGGCCTATATTCA
	Dharmacon	J-012081-07	GGACAGAGTCACAGTAGTC
	Dharmacon	J-012081-08	GTACGGGAGTTTCTTCCTA

confocal microscopy. A FluidFM microchanneled cantilever was approached to the surface of the dish and used to trap individual nanoparticle by applying a steady negative pressure of −800 mbar through the microfluidic system. Using the force control of the Bruker Resolve atomic force microscope, the cantilever with the trapped nanoparticle was then approached to the membrane of individual transfected HeLa cells by applying a 5-nN force that was kept constant after the tip was engaged. In parallel, the focal plane of the confocal microscope was focused on the bead, and 10-min time series were recorded in fast-scanning mode to monitor fluorescence variations in the surroundings of the nanoparticle.

Image analyses and quantifications

Images were processed with Zen blue 3.3 (Zeiss) and Fiji 1.53f51 (National Institutes of Health), and all image quantifications were performed with Fiji. A macro was written to semiautomate fluorescence quantification around each individual nanostructure (see fig.

S3 for a representation of the quantification process). The macro is available upon reasonable request.

For Airyscan images of cells seeded on nanostructured substrates (Figs. 2, A to C, 3, B to F, 4, B, E, G, and H, and 6G and figs. S6, B to F, H, and J, S7, B to F, H, and J, S9, B, D, and F, and S10, B, C, E, and F), ROIs were drawn around cells and a threshold was manually applied to isolate the fluorescence of nanostructures from the background in these ROIs. Next, individual nanostructures were isolated on the basis of their area and circularity using the plugin "Extended Particle Analyzer." The plugin returns the coordinates of the centers of each nanostructure, which were then overlaid on the channel to quantify. When a small drift between channels was observed, centers were realigned accordingly. Then, circular radial profiles were computed in the channels to quantify on the basis of the overlaid nanostructure centers using the plugin "Radial Profile Angle." All individual nanostructures were always analyzed except for nanostructures that were too close to cell edges, which were excluded

from the quantification. These radial profiles represent the average fluorescence intensity at a given distance from the center. Each profile is normalized by the fluorescence intensity at 1 μm from the center of the deformation, which corresponds to the nondeformed/flat plasma membrane (0.5 μm for 100-nm nanostructures). The graph obtained represents the average increase in fluorescence intensity (called enrichment ratio) at a given distance from the center of the nanostructure compared to the flat membrane. Enrichment ratios for each nanostructure were then pooled together, and the average radial intensity profile was calculated. The average normalized intensity at 250, 150, and 50 nm from the center, for 500-, 300-, and 100-nm nanostructures, respectively, was then used to compare various conditions.

For Airyscan time series of cells seeded on nanostructured substrates (Fig. 5, A to E, and fig. S11, A to E), stacks were first corrected for slight drifts during imaging using the plugin "HyperStackReg." Of note, no correction for fluorophore bleaching was made as the enrichment ratios later computed are normalized on each frame. The plugin "Z project" was then used to average the fluorescence intensity of the nanostructures in a single image to refine their signals and to precisely find their centers. The quantification was then done similarly as previously described using the average centers to compute the profiles for each frame around each nanostructure. Quantification was done only on a subset of nanostructures. Nanostructures too close to cell edges were excluded, and a fluctuation of either CDC42, CIP4, LifeAct, or PalMyr signal around membrane deformations was required for their quantifications. Rings around membrane deformations that were stables for the entire duration of the acquisition were not quantified as there is no dynamic to extract. Extracted enrichment ratios over time for each channel were processed by first computing the unweighted moving averages and then correlation coefficients between the two signals for each deformation using JMP Pro v16.0 software.

For Airyscan Z-stacks of cells expressing representative BAR domain proteins from each family (fig. S4A), cropped images of fixed size centered on individual nanostructures were first extracted among multiple cells and images. These cropped areas were then aligned in Z based on the maximum fluorescence intensity of the nanostructures, and the GFP fluorescence intensity was normalized between 0 and 1 across the whole stack. The quantification was then carried out similarly as previously described using nanostructure centers to compute the profiles for each slice. To create heatmaps of each BAR protein, multiple stacks were combined and averaged.

For confocal time series acquired during FluidFM/confocal experiments (Fig. 5F), a circular ROI was defined around the fluorescent bead and the average fluorescence intensity values from the LifeAct channel were extracted from each frame. This average intensity was normalized by the LifeAct signal in a region away from the bead.

Nuclear translocation of STAT1 (Fig. 6, D and E) was quantified with a homemade plugin (60) by calculating the nucleo-cytoplasmic ratio of phospho-STAT1 signal. Nuclei masks were realized because of DAPI staining.

Statistical analyses

All statistical analyses were performed using JMP Pro v16.0 software. To normalize the enrichment ratios into Gaussian distributions, a $\log_{10}$ transformation was systematically applied to the ratios before averaging them. In the case of Gaussian distributions, parametric tests were used, and data were represented on graphs as means ± SEM as error bars. In the case of non-Gaussian distributions, nonparametric tests were used, and data were represented on graphs as median with quartiles. Details on the parametric and nonparametric tests used for each analysis, as well as other statistical details related to specific graphs, are indicated in figure legends. Significance of comparisons is represented on the graphs by asterisks. No statistical method was used to predetermine sample size. For the screening of BAR domain proteins on 500-, 300-, and 100-nm deformations (Fig. 2, A to C), independent experimental repeats were weighted in such a way that each one is equally represented in the pooled dataset.

Supplementary Materials

This PDF file includes:
Figs. S1 to S13
Legends for movies S1 to S14
Legend for table S1

Other Supplementary Material for this manuscript includes the following:
Movies S1 to S14
Table S1

REFERENCES AND NOTES

1. A. I. Teixeira, G. A. Abrams, P. J. Bertics, C. J. Murphy, P. F. Nealey, Epithelial contact guidance on well-defined micro- and nanostructured substrates. *J. Cell Sci.* **116**, 1881–1892 (2003).

2. J. Lu, M. P. Rao, N. C. MacDonald, D. Khang, T. J. Webster, Improved endothelial cell adhesion and proliferation on patterned titanium surfaces with rationally designed, micrometer to nanometer features. *Acta Biomater.* **4**, 192–201 (2008).

3. M. R. Lee, K. W. Kwon, H. Jung, H. N. Kim, K. Y. Suh, K. Kim, K.-S. Kim, Direct differentiation of human embryonic stem cells into selective neurons on nanoscale ridge/groove pattern arrays. *Biomaterials* **31**, 4360–4366 (2010).

4. M. J. Dalby, N. Gadegaard, R. O. C. Oreffo, Harnessing nanotopography and integrin–matrix interactions to influence stem cell fate. *Nat. Mater.* **13**, 558–569 (2014).

5. P.-Y. Wang, P. Thissen, P. Kingshott, Modulation of human multipotent and pluripotent stem cells using surface nanotopographies and surface-immobilised bioactive signals: A review. *Acta Biomater.* **45**, 31–59 (2016).

6. A. Dolatshahi-Pirouz, T. Jensen, D. C. Kraft, M. Foss, P. Kingshott, J. L. Hansen, A. N. Larsen, J. Chevallier, F. Besenbacher, Fibronectin adsorption, cell adhesion, and proliferation on nanostructured tantalum surfaces. *ACS Nano* **4**, 2874–2882 (2010).

7. G. T. Christopherson, H. Song, H.-Q. Mao, The influence of fiber diameter of electrospun substrates on neural stem cell differentiation and proliferation. *Biomaterials* **30**, 556–564 (2009).

8. A. Ray, O. Lee, Z. Win, R. M. Edwards, P. W. Alford, D.-H. Kim, P. P. Provenzano, Anisotropic forces from spatially constrained focal adhesions mediate contact guidance directed cell migration. *Nat. Commun.* **8**, 14923 (2017).

9. A. Ferrari, M. Cecchini, A. Dhawan, S. Micera, I. Tonazzini, R. Stabile, D. Pisignano, F. Beltram, Nanotopographic control of neuronal polarity. *Nano Lett.* **11**, 505–511 (2011).

10. W. Zhao, L. Hanson, H.-Y. Lou, M. Akamatsu, P. D. Chowdary, F. Santoro, J. R. Marks, A. Grassart, D. G. Drubin, Y. Cui, B. Cui, Nanoscale manipulation of membrane curvature for probing endocytosis in live cells. *Nat. Nanotechnol.* **12**, 750–756 (2017).

11. R. C. Cail, C. R. Shirazinejad, D. G. Drubin, Induced nanoscale membrane curvature bypasses the essential endocytic function of clathrin. *J. Cell Biol.* **221**, e202109013 (2022).

12. H.-Y. Lou, W. Zhao, X. Li, L. Duan, A. Powers, M. Akamatsu, F. Santoro, A. F. McGuire, Y. Cui, D. G. Drubin, B. Cui, Membrane curvature underlies actin reorganization in response to nanoscale surface topography. *Proc. Natl. Acad. Sci. U.S.A.* **116**, 23143–23151 (2019).

13. F. Daste, A. Walrant, M. R. Holst, J. R. Gadsby, J. Mason, J.-E. Lee, D. Brook, M. Mettlen, E. Larsson, S. F. Lee, R. Lundmark, J. L. Gallop, Control of actin polymerization via the coincidence of phosphoinositides and high membrane curvature. *J. Cell Biol.* **216**, 3745–3765 (2017).

14. M. Galic, S. Jeong, F.-C. Tsai, L.-M. Joubert, Y. I. Wu, K. M. Hahn, Y. Cui, T. Meyer, External push and internal pull forces recruit curvature-sensing N-BAR domain proteins to the plasma membrane. *Nat. Cell Biol.* **14**, 874–881 (2012).

15. J. L. Gallop, A. Walrant, L. C. Cantley, M. W. Kirschner, Phosphoinositides and membrane curvature switch the mode of actin polymerization via selective recruitment of toca-1 and Snx9. *Proc. Natl. Acad. Sci. U.S.A.* **110**, 7193–7198 (2013).

16. B. J. Peter, H. M. Kent, I. G. Mills, Y. Vallis, P. J. G. Butler, P. R. Evans, H. T. McMahon, BAR domains as sensors of membrane curvature: The amphiphysin BAR structure. *Science* **303**, 495–499 (2004).

17. J. Carlton, M. Bujny, B. J. Peter, V. M. J. Oorschot, A. Rutherford, H. Mellor, J. Klumperman, H. T. McMahon, P. J. Cullen, Sorting nexin-1 Mediates tubular endosome-to-TGN transport through coincidence sensing of high- curvature membranes and 3-phosphoinositides. *Curr. Biol.* **14**, 1791–1800 (2004).

18. C. Mim, V. M. Unger, Membrane curvature and its generation by BAR proteins. *Trends Biochem. Sci.* **37**, 526–533 (2012).

19. W. M. Henne, H. M. Kent, M. G. J. Ford, B. G. Hegde, O. Daumke, P. J. G. Butler, R. Mittal, R. Langen, P. R. Evans, H. T. McMahon, Structure and analysis of FCHo2 F-BAR domain: A dimerizing and membrane recruitment module that effects membrane curvature. *Structure* **15**, 839–852 (2007).

20. A. Frost, P. De Camilli, V. M. Unger, F-BAR proteins join the BAR family fold. *Structure* **15**, 751–753 (2007).

21. L. C. W. Hak, S. Khan, I. Di Meglio, A.-L. Law, S. L.-A. Häsler, L. M. Quintaneiro, A. P. A. Ferreira, M. Krause, H. T. McMahon, E. Boucrot, FBP17 and CIP4 recruit SHIP2 and lamellipodin to prime the plasma membrane for fast endophilin-mediated endocytosis. *Nat. Cell Biol.* **20**, 1023–1031 (2018).

22. F. Baschieri, K. Porshneva, G. Montagnac, Frustrated clathrin-mediated endocytosis—Causes and possible functions. *J. Cell Sci.* **133**, jcs240861 (2020).

23. F. Baschieri, S. Dayot, N. Elkhatib, N. Ly, A. Capmany, K. Schauer, T. Betz, D. M. Vignjevic, R. Poincloux, G. Montagnac, Frustrated endocytosis controls contractility-independent mechanotransduction at clathrin-coated structures. *Nat. Commun.* **9**, 3825 (2018).

24. F. Baschieri, D. Le Devedec, S. Tettarasar, N. Elkhatib, G. Montagnac, Frustration of endocytosis potentiates compression-induced receptor signaling. *J. Cell Sci.* **133**, jcs239681 (2020).

25. S. Degand, G. Lamblin, C. C. Dupont-Gillain, Colloidal lithography using silica particles: Improved particle distribution and tunable wetting properties. *J. Colloid Interface Sci.* **392**, 219–225 (2013).

26. M. Su, Y. Zhuang, X. Miao, Y. Zeng, W. Gao, W. Zhao, M. Wu, Comparative study of curvature sensing mediated by F-BAR and an intrinsically disordered region of FBP17. *iScience* **23**, 101712 (2020).

27. S. Guerrier, J. Coutinho-Budd, T. Sassa, A. Gresset, N. V. Jordan, K. Chen, W.-L. Jin, A. Frost, F. Polleux, The F-BAR domain of srGAP2 induces membrane protrusions required for neuronal migration and morphogenesis. *Cell* **138**, 990–1004 (2009).

28. H.-F. Renard, F. Tyckaert, C. Lo Giudice, T. Hirsch, C. A. Valades-Cruz, C. Lemaigre, M. Shafaq-Zadah, C. Wunder, R. Wattiez, L. Johannes, P. van der Bruggen, D. Alsteens, P. Morsomme, Endophilin-A3 and galectin-8 control the clathrin-independent endocytosis of CD166. *Nat. Commun.* **11**, 1457 (2020).

29. F. Tyckaert, N. Zanin, P. Morsomme, H.-F. Renard, Rac1, the actin cytoskeleton and microtubules are key players in clathrin-independent endophilin-A3-mediated endocytosis. *J. Cell Sci.* **135**, jcs259623 (2022).

30. P. Aspenström, BAR domain proteins regulate Rho GTPase signaling, in *Protein Reviews—Purinergic Receptors. Advances in Experimental Medicine and Biology*, M. Z. Atassi, Ed. (Springer International Publishing, 2019), pp. 33–53.

31. J. R. Watson, H. M. Fox, D. Nietlispach, J. L. Gallop, D. Owen, H. R. Mott, Investigation of the interaction between Cdc42 and its effector TOCA1: Handover OF Cdc42 TO the actin regulator N-wasp is facilitated by differential binding affinities*. *J. Biol. Chem.* **291**, 13875–13890 (2016).

32. J. Saarikangas, H. Zhao, P. Lappalainen, Regulation of the actin cytoskeleton-plasma membrane interplay by phosphoinositides. *Physiol. Rev.* **90**, 259–289 (2010).

33. P. A. Janmey, R. Bucki, R. Radhakrishnan, Regulation of actin assembly by PI(4,5)P2 and other inositol phospholipids: An update on possible mechanisms. *Biochem. Biophys. Res. Commun.* **506**, 307–314 (2018).

34. P. Varnai, B. Thyagarajan, T. Rohacs, T. Balla, Rapidly inducible changes in phosphatidylinositol 4,5-bisphosphate levels influence multiple regulatory functions of the lipid in intact living cells. *J. Cell Biol.* **175**, 377–382 (2006).

35. A. Arcaro, M. P. Wymann, Wortmannin is a potent phosphatidylinositol 3-kinase inhibitor: The role of phosphatidylinositol 3,4,5-trisphosphate in neutrophil responses. *Biochem. J.* **296**, 297–301 (1993).

36. G. R. Chichili, W. Rodgers, Clustering of membrane raft proteins by the actin cytoskeleton. *J. Biol. Chem.* **282**, 36682–36691 (2007).

37. B. P. Head, H. H. Patel, P. A. Insel, Interaction of membrane/lipid rafts with the cytoskeleton: Impact on signaling and function. *Biochim. Biophys. Acta* **1838**, 532–545 (2014).

38. P.-F. Lenne, L. Wawrezinieck, F. Conchonaud, O. Wurtz, A. Boned, X.-J. Guo, H. Rigneault, H.-T. He, D. Marguet, Dynamic molecular confinement in the plasma membrane by micro-domains and the cytoskeleton meshwork. *EMBO J.* **25**, 3245–3256 (2006).

39. E. Sezgin, I. Levental, S. Mayor, C. Eggeling, The mystery of membrane organization: Composition, regulation and roles of lipid rafts. *Nat. Rev. Mol. Cell Biol.* **18**, 361–374 (2017).

40. S. Boulant, C. Kural, J.-C. Zeeh, F. Ubelmann, T. Kirchhausen, Actin dynamics counteract membrane tension during clathrin-mediated endocytosis. *Nat. Cell Biol.* **13**, 1124–1131 (2011).

41. A. Kusumi, T. K. Fujiwara, N. Morone, K. J. Yoshida, R. Chadda, M. Xie, R. S. Kasai, K. G. N. Suzuki, Membrane mechanisms for signal transduction: The coupling of the meso-scale raft domains to membrane-skeleton-induced compartments and dynamic protein complexes. *Semin. Cell Dev. Biol.* **23**, 126–144 (2012).

42. F. Castro, A. P. Cardoso, R. M. Gonçalves, K. Serre, M. J. Oliveira, Interferon-gamma at the crossroads of tumor immune surveillance or evasion. *Front. Immunol.* **9**, (2018).

43. A. Elyasi, I. Voloshyna, S. Ahmed, L. J. Kasselman, J. Behbodikhah, J. De Leon, A. B. Reiss, The role of interferon-γ in cardiovascular disease: An update. *Inflamm. Res.* **69**, 975–988 (2020).

44. C. D. Krause, S. Pestka, Historical developments in the research of interferon receptors. *Cytokine Growth Factor Rev.* **18**, 473–482 (2007).

45. C. M. Blouin, Y. Hamon, P. Gonnord, C. Boularan, J. Kagan, C. Viaris de Lesegno, R. Ruez, S. Mailfert, N. Bertaux, D. Loew, C. Wunder, L. Johannes, G. Vogt, F.-X. Contreras, D. Marguet, J.-L. Casanova, C. Galès, H.-T. He, C. Lamaze, Glycosylation-dependent IFN-γR partitioning in lipid and actin nanodomains is critical for JAK activation. *Cell* **166**, 920–934 (2016).

46. Y. Rao, Q. Ma, A. Vahedi-Faridi, A. Sundborger, A. Pechstein, D. Puchkov, L. Luo, O. Shupliakov, W. Saenger, V. Haucke, Molecular basis for SH3 domain regulation of F-BAR–mediated membrane deformation. *Proc. Natl. Acad. Sci. U.S.A.* **107**, 8213–8218 (2010).

47. A. Frost, R. Perera, A. Roux, K. Spasov, O. Destaing, E. H. Egelman, P. De Camilli, V. M. Unger, Structural basis of membrane invagination by F-BAR domains. *Cell* **132**, 807–817 (2008).

48. Q. Wang, M. V. A. S. Navarro, G. Peng, E. Molinelli, S. Lin Goh, B. L. Judson, K. R. Rajashankar, H. Sondermann, Molecular mechanism of membrane constriction and tubulation mediated by the F-BAR protein Pacsin/Syndapin. *Proc. Natl. Acad. Sci. U.S.A.* **106**, 12700–12705 (2009).

49. S. Gopal, C. Chiappini, J. Penders, V. Leonardo, H. Seong, S. Rothery, Y. Korchev, A. Shevchuk, M. M. Stevens, Porous silicon nanoneedles modulate endocytosis to deliver biological payloads. *Adv. Mater.* **31**, e1806788 (2019).

50. B. K. K. Teo, S.-H. Goh, T. S. Kustandi, W. W. Loh, H. Y. Low, E. K. F. Yim, The effect of micro and nanotopography on endocytosis in drug and gene delivery systems. *Biomaterials* **32**, 9866–9875 (2011).

51. S. Chakraborty, R. Ain, NOSTRIN: A novel modulator of trophoblast giant cell differentiation. *Stem Cell Res.* **31**, 135–146 (2018).

52. N. Richnau, P. Aspenström, RICH, a Rho GTPase-activating protein domain-containing protein involved in signaling by Cdc42 and Rac1. *J. Biol. Chem.* **276**, 35060–35070 (2001).

53. F. Fauchereau, U. Herbrand, P. Chafey, A. Eberth, A. Koulakoff, M.-C. Vinet, M. R. Ahmadian, J. Chelly, P. Billuart, The RhoGAP activity of OPHN1, a new F-actin-binding protein, is negatively controlled by its amino-terminal domain. *Mol. Cell. Neurosci.* **23**, 574–586 (2003).

54. V. Endris, B. Wogatzky, U. Leimer, D. Bartsch, M. Zatyka, F. Latif, E. R. Maher, G. Tariverdian, S. Kirsch, D. Karch, G. A. Rappold, The novel Rho-GTPase activating gene MEGAP/ srGAP3 has a putative role in severe mental retardation. *Proc. Natl. Acad. Sci. U.S.A.* **99**, 11754–11759 (2002).

55. K. Takano, K. Toyooka, S. Suetsugu, EFC/F-BAR proteins and the N-WASP–WIP complex induce membrane curvature-dependent actin polymerization. *EMBO J.* **27**, 2817–2828 (2008).

56. H.-Y. H. Ho, R. Rohatgi, A. M. Lebensohn, J. L. Le Ma, S. P. Gygi, M. W. Kirschner, Toca-1 mediates Cdc42-dependent actin nucleation by activating the N-WASP-WIP complex. *Cell* **118**, 203–216 (2004).

57. R. M. Brunetti, G. Kockelkoren, P. Raghavan, G. R. R. Bell, D. Britain, N. Puri, S. R. Collins, M. D. Leonetti, D. Stamou, O. D. Weiner, WASP integrates substrate topology and cell polarity to guide neutrophil migration. *J. Cell Biol.* **221**, e202104046 (2021).

58. J. B. Vinje, N. A. Guadagno, C. Progida, P. Sikorski, Analysis of actin and focal adhesion organisation in U2OS cells on polymer nanostructures. *Nanoscale Res. Lett.* **16**, 143 (2021).

59. S. Machado, V. Mercier, N. Chiaruttini, LimeSeg: A coarse-grained lipid membrane simulation for 3D image segmentation. *BMC Bioinformatics* **20**, 2 (2019).

60. N. Zanin, C. Viaris de Lesegno, J. Podkalicka, T. Meyer, P. Gonzalez Troncoso, P. Bun, L. Danglot, D. Chmiest, S. Urbé, J. Piehler, C. M. Blouin, C. Lamaze, STAM and Hrs interact sequentially with IFN-α receptor to control spatiotemporal JAK–STAT endosomal activation. *Nat. Cell Biol.* **25**, 425–438 (2023).

61. K. L. Madsen, J. Eriksen, J. Milan-Lobo, D. S. Han, M. Y. Niv, I. Ammendrup-Johnsen, U. Henriksen, V. K. Bhatia, D. Stamou, H. H. Sitte, H. T. McMahon, H. Weinstein, U. Gether,

Membrane localization is critical for activation of the PICK1 BAR domain. *Traffic* **9**, 1327–1343 (2008).

62. H. Yamada, S. Padilla-Parra, S.-J. Park, T. Itoh, M. Chaineau, I. Monaldi, O. Cremona, F. Benfenati, P. De Camilli, M. Coppey-Moisan, M. Tramier, T. Galli, K. Takei, Dynamic interaction of amphiphysin with N-WASP regulates actin assembly. *J. Biol. Chem.* **284**, 34244–34256 (2009).

63. E. Lee, M. Marcucci, L. Daniell, M. Pypaert, O. A. Weisz, G.-C. Ochoa, K. Farsad, M. R. Wenk, P. De Camilli, Amphiphysin 2 (Bin1) and T-tubule biogenesis in muscle. *Science* **297**, 1193–1196 (2002).

64. M. Karbowski, S.-Y. Jeong, R. J. Youle, Endophilin B1 is required for the maintenance of mitochondrial morphology. *J. Cell Biol.* **166**, 1027–1039 (2004).

65. J. Li, P. J. Peters, M. Bai, J. Dai, E. Bos, T. Kirchhausen, K. V. Kandror, V. W. Hsu, An ACAP1-containing clathrin coat complex for endocytic recycling. *J. Cell Biol.* **178**, 453–464 (2007).